Available online at www.sciencedirect.com
SCIENCE DIRECT®
Journal of Computational Physics 212 (2006) 218–246
JOURNAL OF COMPUTATIONAL PHYSICS
www.elsevier.com/locate/jcp

Time-accurate calculation of variable density flows with strong temperature gradients and combustion

Bamdad Lessani, Miltiadis V. Papalexandris *

Département de Mécanique, Université Catholique de Louvain, Place du Levant 2, B-1348 Louvain-la-Neuve, Belgium

Received 15 February 2005; received in revised form 30 June 2005; accepted 1 July 2005
Available online 10 August 2005

Abstract

A time-accurate algorithm is proposed for low Mach number, variable density flows with or without chemical reactions. The algorithm is based on a predictor–corrector time integration scheme that employs a projection method for the momentum equation. A constant-coefficient Poisson equation is solved for the pressure following both the predictor and corrector steps to fully satisfy the continuity equation at each time step. Spatial discretization is performed on a collocated grid system that offers computational simplicity and straightforward extension to curvilinear coordinate systems. To avoid the pressure odd–even decoupling that is typically encountered in such grids, a flux interpolation technique is introduced for the equations governing variable density flows. An important characteristic of the proposed algorithm is that it can be applied to flows in both open and closed domains. Its robustness and accuracy are illustrated with a series of numerical experiments. In particular, we present simulations of non-isothermal, turbulent channel flow as well as simulations of a premixed flame–vortex interaction.

Keywords: Variable density flows; Reacting flows; Low Mach number approximation; Poisson equation; Collocated grid; Large-eddy simulation

1. Introduction

Variable density, low Mach number flows have attracted a lot of interest over the years due to their applicability in numerous natural phenomena and technological processes. Typical examples include meteorological flows, flows with convective and/or conductive heat transfer, premixed and diffusion flames, and

* Corresponding author. Tel.: +32 0 10 47 88 83; fax: +32 0 10 45 26 92.
E-mail address: miltos@term.ucl.ac.be (M.V. Papalexandris).

0021-9991/$ - see front matter © 2005 Elsevier Inc. All rights reserved.
doi:10.1016/j.jcp.2005.07.001

many others. Although in low Mach number flows pressure variations are typically small, density and temperature gradients can be large due to heat transfer and/or heat release from chemical reactions.

A straightforward approach for the numerical treatment of the flows of interest is to implicitly discretize the compressible governing equations in time and modify the resulting (implicit) discrete system of equations by adding a pseudo-time derivative, Jameson [10]. The solution of the implicit system at the new time level is the steady-state solution of this modified system of equations in pseudo-time and could be obtained with an iterative method. For low Mach number flows, different acceleration techniques such as preconditioning, multigrid and residual smoothing, could be used to increase the efficiency of the iterative method, Venkateswaran et al. [28], Lessani et al. [12]. With such an implicit method, one could use a large time-step (not limited by the sound speed) if acoustic waves are not to be solved accurately. This approach, however, is still computationally expensive due to the overhead of the iterative method that is necessary to solve the implicit, discretized system of equations. Therefore, this approach is potentially useful only in cases where a generally low Mach number flow-field contains some small and limited regions of moderate or high Mach numbers. The existence of such regions would then necessitate the use of such a compressible solver.

If the Mach number in the entire flow-field is low, then the so-called low Mach number approximation could be applied to the governing equations. This approximation results in the decoupling of the acoustic modes from the vorticity and entropy modes; see, for example, [4,5,14–16,21–23,26]. The set of equations resulting from the low Mach number approximation may be solved using an extension of the projection method, initially applied to incompressible flows by Chorin [2].

In the projection method, taking the divergence of the discretized momentum equation leads to a Poisson equation for the pressure. In constant density flows, the velocity field $\mathbf{u}$ at any time level n is divergence free, i.e., $\nabla \cdot \mathbf{u}^n = \nabla \cdot \mathbf{u}^{n+1} = 0$. In variable density flows, however, when the divergence is applied to the discrete momentum equations, one has to calculate the divergence of $\rho\mathbf{u}$ at time level $n+1$, $\nabla \cdot (\rho\mathbf{u})^{n+1}$, with ρ being the density of the fluid. This term is generally replaced by the time derivative of the density $\partial\rho/\partial t$, from the continuity equation. The discrete form of this derivative still remains a controversial issue.

Cook and Riley [4] reported that this time derivative was the most destabilizing part of their calculations. They further reported that using a second-order explicit approximation for this derivative, along with a third-order Adams–Bashforth method for the momentum equations, is stable for density ratios up to 3. They also stated that even-ordered approximations to the density time derivative were more stable than odd-ordered ones. However, Charentenay et al. [5] used a third-order backward finite-difference formulation for this derivative in their premixed ozone flame simulation with a density (temperature) ratio of 3.64 and they did not report any stability problems.

On the other hand, Najm et al. [21] proposed a predictor–corrector method for the flows of interest in open domains. They reported that such a method increases the robustness of the algorithm. In particular, they successfully applied their algorithm to the 2D problem of the interaction between a counter-rotating vortex pair and a premixed methane-air flame, with the temperature rising from 300 to 1900 K across the flame. In their approach, the time derivatives of the temperature, density and species mass fractions are calculated from the corresponding balance equations. The new values for the density and species mass fractions are determined using an Adams–Bashforth method at the predictor step and a quasi Crank-Nicolson method at the corrector step. At each step the temperature distribution is calculated from the equation of state. In that approach, however, the computation of the total mass of the system is affected by the discretization errors. This has a profound effect in the numerical solution of the Poisson equation in cases of closed domains, where the total mass of the system has to remain exactly constant. This issue is discussed in detail in the present study.

More recently, Nicoud [22] proposed an algorithm that is based on a mixed Runge–Kutta/Crank–Nicolson time stepping and a variable-coefficient Poisson equation for the pressure. If a variable-coefficient Poisson is used, then one has to approximate $\nabla \cdot \mathbf{u}^{n+1}$, instead of $\nabla \cdot (\rho\mathbf{u})^{n+1}$, on the right-hand side of the

Poisson equation. An expression for the velocity divergence can be directly derived from the governing equations. More specifically, it can be shown that the divergence of the velocity field is inversely proportional to the Reynolds number. (This implies that in the inviscid limit, $Re \to \infty$, the divergence-free constraint of the velocity is recovered). Nicoud [22] also mentioned that the use of a constant-coefficient Poisson solver, although more efficient from a computational point of view, makes the calculations unstable for density (temperature) ratios more than 4.

Finally, Pierce [23] spatially filtered the time derivative of the density, using the test-filter operator of the dynamic procedure for large-eddy simulation (LES) of turbulent flows, Germano et al. [8], Moin et al. [17], and stated that it could greatly improve, but not completely guarantee, the stability of the algorithm. He used an iterative semi-implicit scheme, where only the stiffest terms in each equation are treated implicitly. He reported that according to his experience, flows with weak density variations require two or three iterations, while reacting flows with large density ratios may require four or five iterations.

In the present article, we describe an alternative approach for the development of a robust algorithm for time-accurate calculations of variable density flows with or without chemical reactions. The proposed algorithm solves numerically the low Mach number approximation of the balance equations with a predictor–corrector time integration scheme. This scheme employs a projection method for the momentum equation that results in a constant-coefficient Poisson equation.

Instead of using a staggered grid system, which is the common choice for time accurate calculations, we have adopted a collocated grid. The benefits of employing a collocated grid are computational simplicity and straightforward extension of the method to curvilinear coordinate systems. To avoid the problem of pressure odd–even decoupling, which is commonly encountered in collocated grids, a flux interpolation technique for incompressible flows, Morinishi et al. [18], Rhie and Chow [27], is generalized herein to variable density ones. Numerical experiments conducted in the context of the present study, some of which are presented below, have shown that with a careful treatment of the Poisson equation, the algorithm remains stable for high density (temperature) ratios.

The article is organized as follows. The governing equations and the low Mach number approximation are described in Section 2. The numerical algorithm is described in detail in Section 3. Further, Section 4 contains results of numerical simulations of a non-isothermal, turbulent channel flow and a premixed flame–vortex interaction. Finally, Section 5 contains some general remarks and a discussion of the overall effectiveness of the proposed algorithm for computing variable density flows.

2. Governing equations

In this section, we present the governing equations for the flows of interest and we provide a brief description of the low Mach number approximation.

2.1. Non-dimensional equations

In what follows, a superscript '$\wedge$' denotes a dimensional quantity while a subscript 'ref' denotes a reference quantity. Let us consider a fluid consisting of N chemically reacting species in the absence of body forces and radiation. The reaction mechanism is assumed to involve M elementary reactions. Further, let $\hat{x}_i$, $\hat{t}$, $\hat{\rho}$, $\hat{u}_i$, $\hat{p}$, $\widehat{T}$, denote the ith spatial coordinate, time, density, ith velocity vector component, pressure and temperature, respectively. Further, let $\widehat{Y}_k$, $\Delta\hat{h}_k^0$ and W_k denote the kth species concentration, formation enthalpy and molar weight, respectively. The dynamic viscosity and thermal conductivity of the mixture are denoted by $\hat{\mu}$ and $\hat{\kappa}$, respectively. Also, the mixture specific heats are weighted averages of the specific heats of the species, $\hat{c}_p = \sum_{k=1}^{N} \hat{c}_{p,k}\widehat{Y}_k$ and $\hat{c}_v = \sum_{k=1}^{N} \hat{c}_{v,k}\widehat{Y}_k$.

The above quantities are non-dimensionalized as follows:

$$x_i = \hat{x}_i/L_{\text{ref}}, \quad t = \hat{t}u_{\text{ref}}/L_{\text{ref}}, \tag{1}$$

$$\rho = \hat{\rho}/\rho_{\text{ref}}, \quad u_i = \hat{u}_i/u_{\text{ref}}, \quad p = \hat{p}/(\rho_{\text{ref}}u_{\text{ref}}^2), \quad T = \widehat{T}/T_{\text{ref}}, \tag{2}$$

$$\mu = \hat{\mu}/\mu(T_{\text{ref}}), \quad \kappa = \hat{\kappa}/\kappa(T_{\text{ref}}), \tag{3}$$

$$c_p = \hat{c}_p/c_p(T_{\text{ref}}), \quad c_v = \hat{c}_v/c_v(T_{\text{ref}}), \tag{4}$$

$$Y_k = \hat{Y}_k/Y_{k,\text{ref}}, \quad \Delta h_k^0 = \Delta\hat{h}_k^0/(c_p(T_{\text{ref}})T_{\text{ref}}), \qquad k = 1, \ldots, N. \tag{5}$$

The Prandtl number, Pr, Reynolds number, Re and Mach number, M, of the flow are defined with respect to the reference values. Therefore,

$$Pr = \frac{\mu(T_{\text{ref}})c_p(T_{\text{ref}})}{\kappa(T_{\text{ref}})}, \quad Re = \frac{\rho_{\text{ref}}u_{\text{ref}}L_{\text{ref}}}{\mu(T_{\text{ref}})}, \quad M = \frac{u_{\text{ref}}}{\sqrt{\gamma T_{\text{ref}}\mathscr{R}/\overline{W}}}, \tag{6}$$

respectively. In the definition of the Mach number above, γ is the ratio of specific heats at the reference temperature, $\gamma = c_p(T_{\text{ref}})/c_v(T_{\text{ref}})$, $\mathscr{R}$ is the universal gas constant and $\overline{W}$ is the mean molecular weight of the mixture, $\overline{W} = (\sum_{k=1}^{N} Y_k/W_k)^{-1}$.

The mixture is assumed to be a perfect gas and its equation of state is written as

$$p = \frac{\rho T}{\gamma M^2}. \tag{7}$$

For the sake of computational efficiency it is assumed that the Nth species is dominant so far as transport properties are concerned. Therefore, the mixture transport properties are the same as those of the dominant species. A simplified Sutherland law is used for the dimensionless thermal conductivity κ and dynamic viscosity μ,

$$\mu = \kappa = T^{0.7}. \tag{8}$$

The assumption that the Nth species is dominant so far as transport properties are concerned also implies that mass diffusion between any two species k and j ($k \neq N, j \neq N$) is negligible. It is further assumed that the diffusivities $\mathscr{D}_{kN}$ between species k and N are all equal (henceforth denoted by $\mathscr{D}_N$), and that the specific heats of each species $c_{p,k}$ are all equal (henceforth denoted by c_p), as well.

Under the above assumption, the Lewis numbers of the species are all equal, henceforth denoted by Le. Finally, for computational simplicity, it is assumed that the Lewis number equals unity, i.e., $Le = \kappa/(\rho c_p \mathscr{D}_N) = 1$. Therefore, in the terms that describe Fickian diffusion, the product $\rho\mathscr{D}_N$ is replaced by the ratio κ/c_p and the Schmidt number is replaced by the Prandtl number. With these assumptions in mind, the mass, momentum, energy and species balance equations are written in index notation as

$$\frac{\partial\rho}{\partial t} + \frac{\partial\rho u_i}{\partial x_i} = 0, \tag{9}$$

$$\frac{\partial\rho u_i}{\partial t} + \frac{\partial\rho u_i u_j}{\partial x_j} = -\frac{\partial p}{\partial x_i} + \frac{1}{Re}\frac{\partial\sigma_{ij}}{\partial x_j}, \tag{10}$$

$$\rho c_p\frac{\partial T}{\partial t} + \rho c_p u_j\frac{\partial T}{\partial x_j} - (\gamma-1)M^2\left(\frac{\partial p}{\partial t} + u_i\frac{\partial p}{\partial x_i}\right) = \frac{1}{RePr}\frac{\partial}{\partial x_j}\left(\kappa\frac{\partial T}{\partial x_j}\right) + \frac{\gamma-1}{Re}M^2\sigma_{ij}\frac{\partial u_i}{\partial x_j} + \sum_{k=1}^{N} h_k\dot{w}_k, \tag{11}$$

$$\rho\frac{\partial Y_k}{\partial t} + \rho u_j\frac{\partial Y_k}{\partial x_j} = \frac{1}{RePr}\frac{\partial}{\partial x_j}\left(\frac{\kappa}{c_p}\frac{\partial Y_k}{\partial x_j}\right) - \dot{w}_k, \quad k = 1, \ldots, N-1. \tag{12}$$

In the energy and momentum equations above, σ_{ij} is the viscous stress tensor, given by

$$\sigma_{ij} = \mu\left(\frac{\partial u_i}{\partial x_j} + \frac{\partial u_j}{\partial x_i} - \frac{2}{3}\delta_{ij}\frac{\partial u_k}{\partial x_k}\right). \tag{13}$$

Also in the energy equation, h_k is the specific enthalpy of the kth species, $h_k = \Delta h_k^0 + \int_0^T c_{p,k}\mathrm{d}T$ and $\dot{w}_k$ are the chemical source terms for each species. These source terms are generally given by $\dot{w}_k = \sum_{l=1}^{M}\dot{w}_{kl}$ with $\dot{w}_{kl}$ being the mass rate of production per unit volume of the kth species by the lth reaction. When the specific heats under constant pressure are equal for all species, then $\sum_{k=1}^{N} h_k\dot{w}_k = \sum_{k=1}^{N}\Delta h_k^0\dot{w}_k$; see, Poinsot and Veynante [24].

2.2. Low Mach number approximation

The low Mach number equations are derived by expanding the flow variables of the governing equations (9)–(12) as power series in $\varepsilon = \gamma M^2 \ll 1$, with M being the Mach number (see also [4,14,26]),

$$\begin{aligned}
&\rho = \rho^{(0)} + \varepsilon\rho^{(1)} + \cdots,\\
&u_i = u_i^{(0)} + \varepsilon u_i^{(1)} + \cdots,\\
&T = T^{(0)} + \varepsilon T^{(1)} + \cdots,\\
&Y_k = Y_k^{(0)} + \varepsilon Y_k^{(1)} + \cdots, k = 1,\ldots,N,\\
&p = \frac{\rho T}{\gamma M^2} = \frac{1}{\varepsilon}p^{(0)} + p^{(1)} + \cdots
\end{aligned} \tag{14}$$

Substituting these expansions into the conservation equations (9)–(12), and into the ideal gas law (7), and subsequently collecting the lowest order terms in ε, we finally arrive at the low Mach number approximation equations

$$\frac{\partial\rho^{(0)}}{\partial t} + \frac{\partial\rho^{(0)}u_i^{(0)}}{\partial x_i} = 0, \tag{15}$$

$$\frac{\partial\rho^{(0)}u_i^{(0)}}{\partial t} + \frac{\partial\rho u_i^{(0)}u_j^{(0)}}{\partial x_j} = -\frac{\partial p^{(1)}}{\partial x_i} + \frac{1}{Re}\frac{\partial\sigma_{ij}^{(0)}}{\partial x_j}, \tag{16}$$

$$\rho^{(0)}c_p\frac{\partial T^{(0)}}{\partial t} + \rho^{(0)}c_p u_j^{(0)}\frac{\partial T^{(0)}}{\partial x_j} = \frac{1}{RePr}\frac{\partial}{\partial x_j}\left(\kappa\frac{\partial T^{(0)}}{\partial x_j}\right) + \frac{\gamma-1}{\gamma}\frac{\mathrm{d}p^{(0)}}{\mathrm{d}t} + \sum_{k=1}^{N}\Delta h_k^0\dot{w}_k, \tag{17}$$

$$\rho^{(0)}\frac{\partial Y_k^{(0)}}{\partial t} + \rho^{(0)}u_j^{(0)}\frac{\partial Y_k^{(0)}}{\partial x_j} = \frac{1}{RePr}\frac{\partial}{\partial x_j}\left(\frac{\kappa}{c_p}\frac{\partial Y_k^{(0)}}{\partial x_j}\right) - \dot{w}_k^{(0)}, \quad k = 1,\ldots,N-1, \tag{18}$$

$$\frac{\partial p^{(0)}}{\partial x_i} = 0, \tag{19}$$

$$p^{(0)} = \rho^{(0)}T^{(0)}. \tag{20}$$

Eq. (20) is obtained directly by inserting the expansions for ρ and T into the expansion of p, cf. (14). We observe that the pressure field is decomposed into a spatially uniform component $p^{(0)}$ which is interpreted as the thermodynamic pressure, and a variable component $p^{(1)}$, interpreted as the dynamic pressure.

As regards the evolution of $p^{(0)}$, the following three cases are possible: (i) the system is open, (ii) the system is closed and (iii) the system is semi-open so that there is a restricted opening (for example, a crack) between the flow domain and its exterior. In the case of an open system $p^{(0)}$ is constant and equal to the open boundary pressure. For a closed system, $p^{(0)}$ may vary in time but the total mass remains constant

and equals the volume integral of the density, $M_0 = \int \rho^{(0)} \mathrm{d}V$. Then, by dividing the two sides of (20) by $T^{(0)}$ and integrating over the volume V, the following expression for $p^{(0)}$ is readily obtained,

$$p^{(0)} = \frac{M_0}{\int \frac{\mathrm{d}V}{T^{(0)}}}. \tag{21}$$

For the case of a semi-open system, by combining Eqs. (15), (17) and (20) and integrating the resulting equation over the computational domain V, the following ordinary differential equation for $p^{(0)}$ may be obtained (see Rehm et al. [26], Nicoud [22] for details),

$$\frac{\mathrm{d}p^{(0)}}{\mathrm{d}t} = \frac{1}{\int \left(\frac{\gamma-1}{\gamma} - c_p\right) \mathrm{d}V} \left[\frac{-1}{RePr} \int \frac{\partial}{\partial x_j} \left(\kappa \frac{\partial T^{(0)}}{\partial x_j} \right) \mathrm{d}V - \int \sum_{k=1}^{N} \Delta h_k^0 \dot{w}_k \mathrm{d}V + p^{(0)} \int c_p \frac{\partial u_i^{(0)}}{\partial x_i} \mathrm{d}V \right]. \tag{22}$$

Even though this case can be easily incorporated into the proposed numerical algorithm, in the present study we focus our attention to open or closed systems.

3. Numerical method

The proposed numerical method is based on a predictor–corrector method to march in time. As mentioned earlier, this method can be applied to open as well as closed domains. Then, $p^{(0)}$ is either constant or is calculated from Eq. (21). The second term in the expansion of the pressure, $p^{(1)}$, can be calculated by a projection method which is described in detail herein. It is interesting to mention that a predictor–corrector scheme had previously been adopted for the flows of interest in [21]. However, the method presented in [21] was designed for open domains only. For the sake of clarity, the superscripts (0) and (1) will henceforth be dropped, except to distinguish between $p^{(0)}$ and $p^{(1)}$.

3.1. Predictor–corrector projection scheme

In this subsection, the structure of the time integration algorithm is discussed in detail. The time step is Δt with $t_{n+1} = t_n + \Delta t$. Superscripts n, $*$ and $n+1$ denote the known values at the time level n, the predicted or intermediate values and the values at the next time level $n+1$, respectively. As already mentioned, the algorithm consists of two stages, the corrector and the predictor stages, respectively.

3.1.1. Predictor

(i) The predicted value for the temperature, T^*, is calculated from Eq. (17) based on the previous values at time level n,

$$\rho^n c_p \frac{T^* - T^n}{\Delta t} = \mathrm{Res}_T(\rho^n, \mathbf{u}^n, T^n) + \frac{\gamma - 1}{\gamma} \frac{p^{(0)n} - p^{(0)n-1}}{\Delta t} + \sum_{k=1}^{k=N} \Delta h_k^0 \dot{w}_k(\rho^n, Y_k^n, T^n). \tag{23}$$

In the equation above $\mathbf{u} = (u_1, u_2, u_3)$ is the velocity vector and Res_T is the sum of the following convective and heat-transfer residuals,

$$\mathrm{Res}_T = -\rho c_p u_j \frac{\partial T}{\partial x_j} + \frac{1}{RePr} \frac{\partial}{\partial x_j} \left(\kappa \frac{\partial T}{\partial x_j} \right). \tag{24}$$

(ii) For closed systems, the predicted value for the thermodynamic pressure $p^{(0)*}$, is calculated from Eq. (21),

$$p^{(0)*} = \frac{M_0}{\int \frac{dV}{T^*}}. \tag{25}$$

For open systems, however, this equation is no longer valid. In these cases, $p^{(0)*}$ is set equal to the open boundary pressure.

(iii) The predicted value for the density, ρ^*, is evaluated from Eq. (20) which connects the first-order terms of the expansions of the thermodynamic variables,

$$\rho^* = \frac{p^{(0)*}}{T^*}. \tag{26}$$

(iv) In this step, predictions for the velocity vector and the dynamic pressure are calculated. An Adams–Bashforth method is used for the momentum equation (16),

$$\frac{\rho^*\mathbf{u}^* - \rho^n\mathbf{u}^n}{\Delta t} = \frac{3}{2}\mathrm{Res}_u(\rho^n, \mathbf{u}^n) - \frac{1}{2}\mathrm{Res}_u(\rho^{n-1}, \mathbf{u}^{n-1}) - \frac{\partial p^{(1)*}}{\partial x_i}, \tag{27}$$

where Res_u is the sum of the following convective and viscous residuals,

$$\mathrm{Res}_u = -\frac{\partial \rho u_i u_j}{\partial x_j} + \frac{1}{Re}\frac{\partial \sigma_{ij}}{\partial x_j}. \tag{28}$$

Taking the divergence of (27) gives,

$$\nabla\cdot\left(\frac{\rho^*\mathbf{u}^*}{\Delta t}\right) - \nabla\cdot\left(\frac{\rho^*\tilde{\mathbf{u}}}{\Delta t}\right) = -\nabla^2 p^{(1)*}, \tag{29}$$

with,

$$\frac{\rho^*\tilde{\mathbf{u}}}{\Delta t} \equiv \frac{\rho^n\mathbf{u}^n}{\Delta t} + \frac{3}{2}\mathrm{Res}_u(\rho^n, \mathbf{u}^n) - \frac{1}{2}\mathrm{Res}_u(\rho^{n-1}, \mathbf{u}^{n-1}). \tag{30}$$

From the continuity equation (15), the term $\nabla\cdot(\rho^*\mathbf{u}^*)$ equals the time derivative of the density, $(\partial\rho/\partial t)^*$. A second-order approximation is used for this derivative,

$$\nabla\cdot(\rho^*\mathbf{u}^*) = -\left(\frac{\partial\rho}{\partial t}\right)^* = -\frac{3\rho^* - 4\rho^n + \rho^{n-1}}{2\Delta t}. \tag{31}$$

The predicted value of the dynamic pressure $p^{(1)*}$ is computed by inserting (30) and (31) into (29) and solving numerically the resulting constant-coefficient Poisson equation. Having computed $p^{(1)*}$, the predicted value of the velocity vector $\mathbf{u}^*$ is calculated from (27).

(v) The predicted values for the species concentration, Y_k^*, are obtained from Eq. (18) in a way that is similar to the one that was used to get the prediction of the temperature in step i,

$$\rho^*\frac{Y_k^* - Y_k^n}{\Delta t} = \mathrm{Res}_{Y_k}(\rho^*, \mathbf{u}^*, Y_k^n) - \dot{w}_k(\rho^*, Y_k^n, T^*), \quad k = 1, \ldots, N-1, \tag{32}$$

with Res_{Y_k} being the sum of the following convective and mass-diffusion residuals:

$$\mathrm{Res}_{Y_k} = -\rho u_j\frac{\partial Y_k}{\partial x_j} + \frac{1}{RePr}\frac{\partial}{\partial x_j}\left(\frac{\kappa}{c_p}\frac{\partial Y_k}{\partial x_j}\right). \tag{33}$$

3.1.2. Corrector

(i) The temperature at the new time level $n+1$, T^{n+1}, is calculated from Eq. (17) based on the values computed in the predictor stage,

$$\rho^* c_p \frac{T^{n+1}-T^n}{\Delta t} = \mathrm{Res}_T(\rho^*, \mathbf{u}^*, T_{\mathrm{av}}) + \frac{\gamma-1}{\gamma}\frac{p^{(0)n}-p^{(0)n-1}}{\Delta t} + \sum_{k=1}^{k=N} \Delta h_k^0 \dot{w}_k(\rho^*, Y_k^*, T_{\mathrm{av}}), \tag{34}$$

with $T_{\mathrm{av}} = (T^n + T^*)/2$.

(ii) If the domain is closed the thermodynamic pressure $p^{(0)n+1}$ is calculated by

$$p^{(0)n+1} = \frac{M_0}{\int \frac{\mathrm{d}V}{T^{n+1}}}. \tag{35}$$

If the domain is open, $p^{(0)n+1}$ is set equal to the open boundary pressure.

(iii) The density ρ^{n+1} at time level $n+1$ is calculated by

$$\rho^{n+1} = \frac{p^{(0)n+1}}{T^{n+1}}. \tag{36}$$

(iv) In this step, the velocity vector at the new time level $n+1$ is determined from the momentum equation (16),

$$\frac{\rho^{n+1}\mathbf{u}^{n+1}-\rho^n\mathbf{u}^n}{\Delta t} = \frac{3}{2}\mathrm{Res}_u(\rho^n, \mathbf{u}^n) - \frac{1}{2}\mathrm{Res}_u(\rho^{n-1}, \mathbf{u}^{n-1}) - \frac{\partial p^{(1)n+1}}{\partial x_i}. \tag{37}$$

Further, taking the divergence of (37) gives,

$$\nabla\cdot\left(\frac{\rho^{n+1}\mathbf{u}^{n+1}}{\Delta t}\right) - \nabla\cdot\left(\frac{\rho^{n+1}\breve{\mathbf{u}}}{\Delta t}\right) = -\nabla^2 p^{(1)n+1}, \tag{38}$$

with,

$$\frac{\rho^{n+1}\breve{\mathbf{u}}}{\Delta t} = \frac{\rho^n\mathbf{u}^n}{\Delta t} + \frac{3}{2}\mathrm{Res}_u(\rho^n, \mathbf{u}^n) - \frac{1}{2}\mathrm{Res}_u(\rho^{n-1}, \mathbf{u}^{n-1}). \tag{39}$$

From the continuity equation (15), the term $\nabla\cdot(\rho^{n+1}\mathbf{u}^{n+1})$ equals the time derivative of the density $(\partial\rho/\partial t)^{n+1}$. As in the predictor stage, a second-order approximation is used for this derivative,

$$\nabla\cdot(\rho^{n+1}\mathbf{u}^{n+1}) = -\left(\frac{\partial\rho}{\partial t}\right)^{n+1} = -\frac{3\rho^{n+1}-4\rho^n+\rho^{n-1}}{2\Delta t}. \tag{40}$$

The velocity vector $\mathbf{u}^{n+1}$ is evaluated from (37), while the dynamic pressure $p^{(1)n+1}$ is computed by inserting (39) and (40) into (38) and, subsequently, solving the resulting equation with a Poisson solver.

(v) Based on the final values of the density, velocity and temperature, the species equation (18) is updated,

$$\rho^{n+1}\frac{Y_k^{n+1}-Y_k^n}{\Delta t} = \mathrm{Res}_{Y_k}(\rho^{n+1}, \mathbf{u}^{n+1}, Y_k^{\mathrm{av}}) - \dot{w}_k(\rho^{n+1}, Y_k^{\mathrm{av}}, T^{n+1}), \quad k = 1, \ldots, N-1, \tag{41}$$

with $Y_k^{\mathrm{av}} = (Y_k^n + Y_k^*)/2$.

(vi) The temperature equation is reintegrated from time t_n to t_{n+1}, with the same two-stage method using the final values of the density and velocity. In other words, the following operations are performed,

$$\rho^{n+1}c_p\frac{T^*-T^n}{\Delta t} = \mathrm{Res}_T(\rho^{n+1}, \mathbf{u}^{n+1}, T^n) + \frac{\gamma-1}{\gamma}\frac{p^{(0)n}-p^{(0)n-1}}{\Delta t} + \sum_{k=1}^{k=N}\Delta h_k^0\dot{w}_k(\rho^{n+1}, Y_k^{n+1}, T^n) \tag{42}$$

and

$$\rho^{n+1}c_p\frac{T^{n+1}-T^n}{\Delta t}=\mathrm{Res}_T(\rho^{n+1},\mathbf{u}^{n+1},T_{\mathrm{av}})+\frac{\gamma-1}{\gamma}\frac{p^{(0)n}-p^{(0)n-1}}{\Delta t}+\sum_{k=1}^{k=N}\Delta h_k^0\dot{w}_k(\rho^{n+1},Y_k^{n+1},T_{\mathrm{av}}) \tag{43}$$

with $T_{\mathrm{av}}=(T^n+T^*)/2$.

The motivation for step (vi), cf. (42) and (43), came from numerical experiments on LES of non-isothermal, turbulent channel flow. To fix ideas, let us consider flow between two walls that are maintained at different temperatures and let q_{h} be the heat flux from the hot wall to the fluid and q_{c} the heat flux from the fluid to the cold wall. In a statistically stationary flow, the time average of $q_{\mathrm{h}}-q_{\mathrm{c}}$ should be zero. However, in our simulations it was observed that, without this additional operation, the time average of $q_{\mathrm{h}}-q_{\mathrm{c}}$ would take a non-zero value. This is an energy conservation error and, as our numerical tests showed, can be reduced substantially by the additional calculation of (42) and (43). For example, in channel flow with wall temperature ratio equal to 9, the error on the time average of $(q_{\mathrm{h}}-q_{\mathrm{c}})/q_{\mathrm{c}}$ dropped from 0.187 to 0.039 by employing the additional calculation of the energy equation.

Essentially this re-integration of the energy equation can be generalized to an outer iteration loop for all balance equations. Such iterative procedures have been employed in [9,23]. In our test cases, the error in the time average of $(q_{\mathrm{h}}-q_{\mathrm{c}})/q_{\mathrm{c}}$ was sufficiently small after completion of step (vi) and, therefore, the full outer iteration loop was not employed for computational savings. At this point, however, we can not exclude the possibility that the full loop might be necessary for certain flow cases.

Further, in Eqs. (30) and (39) an explicit formulation for $\tilde{\mathbf{u}}$ and $\breve{\mathbf{u}}$ is used. In the explicit formulation, the right-hand sides of these two equations are the same, therefore, in the computer code there is no need for these two equations to be calculated twice. However, for some test cases like the non-isothermal channel flow with a non-uniform mesh in one direction, an implicit treatment of the transport terms in that specific direction would increase the allowable time step of the calculation. If an implicit treatment of $\tilde{\mathbf{u}}$ and $\breve{\mathbf{u}}$ is chosen, then the right-hand sides of (30) and (39) would be different. We therefore conclude that, depending on the application, Eqs. (30) and (39) might need to be calculated separately.

It is also worth mentioning that in some earlier works, [4,22,23], the authors reported stability problems triggered by the pressure Poisson equation. However, in our test cases no such stability problems were observed with the algorithm proposed herein. The robustness of the present algorithm can be attributed to the following elements: (i) the use of a predictor–corrector time-marching technique, (ii) the use of the balance equations to evaluate the flow variables and not their time-derivatives (as done in [21], for example) and, (iii) the particular sequence in the calculation of the thermodynamic variables that is embedded in the time-marching technique. According to this sequence, the temperature is calculated first from the energy equation, followed by the calculation of the thermodynamic pressure from (21) and, subsequently, by the calculation of the density from (20).

The combined use of elements ii and iii above has a clear advantage, at least for flows in closed domains. To be more specific, if we consider the predictor stage, the solvability conditions of the pressure Poisson equation, with the boundary conditions mentioned above, imply that the volume integral of the left-hand side of equation (29) must be equal to zero, i.e.,

$$\int\nabla\cdot(\rho^*\mathbf{u}^*)\mathrm{d}V-\int\nabla\cdot(\rho^*\tilde{\mathbf{u}})\mathrm{d}V=0. \tag{44}$$

Similarly, the volume integral of the left-hand side of (38) in the corrector stage must also be zero. For a closed system, the sequence with which the flow variables are calculated in the present scheme ensures that at each step we have

$$\int\rho^*\mathrm{d}V=\int\rho^n\mathrm{d}V=\int\rho^{n\pm1}\mathrm{d}V=M_0. \tag{45}$$

Therefore, from Eq. (31), the first integral in Eq. (44) is equal to zero, i.e., $\int \nabla \cdot (\rho^* \mathbf{u}^*) \mathrm{d}V = 0$. The second integral in Eq. (44) is also equal to zero, by virtue of the Gauss's theorem and the fact that the $\tilde{u}$ is zero at the solid walls, (the same holds if periodic boundary conditions are used instead of the solid walls). Consequently, condition (44) is always satisfied to machine accuracy.

On the other hand, in an open system the total mass may not be constant. Therefore, the two integrals in the left-hand side of (44) may not be simultaneously equal to zero. Even so, in the present algorithm, the value for $\tilde{u}$ at the outflow boundary is still set in a way that the solvability condition (44) is satisfied. In the numerical tests that we conducted for validation purposes we did not observe any stability problems arising from this choice of outflow condition for $\tilde{u}$. Nonetheless, the possibility to encounter such stability problems for certain type of flows can not be excluded at this time.

Further, it is important to mention that, because of the need to specify boundary conditions for $\tilde{u}$, it is not possible to implement non-reflecting outlet boundary conditions in a straightforward manner with the proposed algorithm. This is a weakness of the algorithm because it implies that outlet boundaries of the computational domains have to be taken sufficiently far, i.e., in regions of the flow where the spatial derivatives of the flow variables are very small.

The proposed time-integration method has been tested in a series of flow problems with strong temperature gradients, some of which are presented in Section 4 below. In these tests, the algorithm was found capable of successfully predicting flows with strong temperature and density gradients. (For example, in non-isothermal channel flows, the algorithm could handle wall-temperature ratios as high as 9, at least). This by no means implies that the proposed method can handle arbitrarily large density or temperature gradients. In fact, it is expected that if these gradients become sufficiently large, then the algorithm will break. The limit of temperature gradients at which the algorithm breaks depends, of course, in the spatial and temporal resolution as well as the Reynolds, Prandtl and Schmidt numbers of the flow.

3.2. Spatial discretization in a collocated grid system

In this section, we describe the spatial discretization scheme for the governing equations (15)–(18). As mentioned in the Section 1, the proposed algorithm employs a collocated grid system. As mentioned in the Section 1, the advantages of collocated grids over staggered ones are computational simplicity and straightforward extension of the method to curvilinear coordinate systems. On the other hand, particular attention should be paid to the fact that collocated grids can produce spurious oscillations of the pressure field. This problem is known in the literature as *odd–even decoupling*. It has been shown that for incompressible flows the pressure odd–even decoupling of collocated grids can be remedied with a flux interpolation method, [18,27]. Herein this method is generalized to variable density flows.

First, all second-order differential operators that model transport phenomena (viscosity, heat conduction and mass diffusion) are discretized using second-order central differences. The discretization of the convective terms is achieved via the introduction of the following three auxiliary scalar fluxes

$$F_i \equiv \rho u_i, \quad i = 1, 2, 3, \tag{46}$$

which are staggered with respect to other variables in space. This implies that each auxiliary flux F_i is defined on the center of the cell interface that is normal to the x_i direction, whereas all flow quantities are evaluated at the centers of the computational cells. The auxiliary fluxes are calculated via interpolation. By convention, these fluxes are assigned the same indices with the associated computational cell.

In the discussion that follows we will use extensively two discrete operators, the finite-difference and the interpolation operators. Their definition is as follows. If Δx_1 is the grid spacing in the x_1 direction, the general finite-difference operator acting on $\phi(x_1, x_2, x_3)$ in the x_1 direction is defined as

$$\frac{\delta_n \phi(x_1, x_2, x_3)}{\delta_n x_1} = \frac{\phi(x_1 + n\frac{\Delta x_1}{2}, x_2, x_3) - \phi(x_1 - n\frac{\Delta x_1}{2}, x_2, x_3)}{n\Delta x_1}. \tag{47}$$

Completely similar definitions hold for the operator acting in the x_2 and x_3 directions. The general interpolation operator acting on the x_1 direction is defined as

$$\bar{\phi}^{nx_1}(x_1,x_2,x_3) = \frac{\phi(x_1 + n\frac{\Delta x_1}{2}, x_2, x_3) + \phi(x_1 - n\frac{\Delta x_1}{2}, x_2, x_3)}{2}, \tag{48}$$

with similar definitions for the operator acting on the other two spatial directions.

3.2.1. Second-order schemes

In accordance with the proposed time marching technique that was described above, one has to compute the auxiliary fluxes in both the predictor as well as in the corrector stage. This means that one has to compute F_i^* and F_i^{n+1} in addition to the velocities u^* and $\mathbf{u}^{n+1}$. In the predictor step, F_i^* is evaluated from Eq. (27) combined with an interpolation for $\rho^* \tilde{u}_i$ in the x_i direction, cf. (30). This results in the following expression:

$$F_i^* = \overline{\rho^* \tilde{u}_i}^{1x_i} - \Delta t \frac{\delta_1 p^{(1)*}}{\delta_1 x_i}. \tag{49}$$

It is worth clarifying that the discrete operators that appear in the above equation act on the same points as the auxiliary fluxes themselves. Further, let I, J and K denote the indices of a given computational cell in the x_1, x_2 and x_3 directions, respectively. Then, by using (49), the following expressions for the auxiliary fluxes F_i are obtained:

$$F^*_{1_{I,J,K}} = \frac{\rho^*_{I,J,K}\tilde{u}_{1_{I,J,K}} + \rho^*_{I+1,J,K}\tilde{u}_{1_{I+1,J,K}}}{2} - \Delta t \frac{p^{(1)*}_{I+1,J,K} - p^{(1)*}_{I,J,K}}{\Delta x_1}, \tag{50}$$

$$F^*_{2_{I,J,K}} = \frac{\rho^*_{I,J,K}\tilde{u}_{2_{I,J,K}} + \rho^*_{I,J+1,K}\tilde{u}_{2_{I,j+1,K}}}{2} - \Delta t \frac{p^{(1)*}_{I,J+1,K} - p^{(1)*}_{I,J,K}}{\Delta x_2}, \tag{51}$$

$$F^*_{3_{I,J,K}} = \frac{\rho^*_{I,J,K}\tilde{u}_{3_{I,J,K}} + \rho^*_{I,j,K+1}\tilde{u}_{3_{I,j,K+1}}}{2} - \Delta t \frac{p^{(1)*}_{I,J,K+1} - p^{(1)*}_{I,J,K}}{\Delta x_3}. \tag{52}$$

Similarly, for the corrector stage, the expressions for the auxiliary fluxes F_i^{n+1} are obtained from Eq. (37) combined with an interpolation for the term $\rho^{n+1}\breve{u}_i$, cf. (39),

$$F_i^{n+1} = \overline{\rho^{n+1}\breve{u}_i}^{1x_i} - \Delta t \frac{\delta_1 p^{(1)n+1}}{\delta_1 x_i}. \tag{53}$$

By expanding this relation we can arrive at expressions of F_i^{n+1} that are analogous to Eqs. (50)–(52), above.

Once the auxiliary fluxes are known, the velocity vectors $\mathbf{u}^*$ and $\mathbf{u}^{n+1}$, which are collocated with the pressure, are calculated from Eqs. (27) and (37), respectively:

$$u_i^* = \frac{1}{\rho^*}\left(\rho^*\tilde{u}_i - \Delta t \frac{\delta_2 p^{(1)*}}{\delta_2 x_i}\right), \tag{54}$$

$$u_i^{n+1} = \frac{1}{\rho^{n+1}}\left(\rho^{n+1}\breve{u}_i - \Delta t \frac{\delta_2 p^{(1)n+1}}{\delta_2 x_i}\right). \tag{55}$$

Further, Eq. (31) of the predictor stage, which arises from the temporal discretization of the continuity equation (15), can be discretized in space by employing the auxiliary fluxes F_i instead of centered finite-differences at the collocated points. This results in

$$\frac{3\rho^* - 4\rho^n + \rho^{n-1}}{2\Delta t} + \frac{\delta_1 F_i^*}{\delta_1 x_i} = 0. \tag{56}$$

Similarly, the discretization of that appears in (40) of the corrector stage is

$$\frac{3\rho^{n+1}-4\rho^{n}+\rho^{n-1}}{2\Delta t}+\frac{\delta_1 F_i^{n+1}}{\delta_1 x_i}=0. \tag{57}$$

Also, spatial discretization of Eqs. (29) and (38) can be obtained by applying the δ_1 discrete finite-difference operator (47) in Eqs. (49) and (53), respectively. The emerging equations that arise contain the divergence term $\delta_1 F_i/\delta_1 x_i$. An expression for this term can be obtained directly by (56) and (57) above. Thus, we finally arrive at the following discretization of the Poisson equations (29) and (38):

$$\frac{3\rho^{*}-4\rho^{n}+\rho^{n-1}}{2\Delta t}+\frac{\delta_1 \overline{\rho^{*}\tilde{u}_i}^{1x_i}}{\delta_1 x_i}=\Delta t\frac{\delta_1}{\delta_1 x_i}\left(\frac{\delta_1 p^{(1)*}}{\delta_1 x_i}\right), \tag{58}$$

$$\frac{3\rho^{n+1}-4\rho^{n}+\rho^{n-1}}{2\Delta t}+\frac{\delta_1 \overline{\rho^{n+1}\breve{u}_i}^{1x_i}}{\delta_1 x_i}=\Delta t\frac{\delta_1}{\delta_1 x_i}\left(\frac{\delta_1 p^{(1)n+1}}{\delta_1 x_i}\right). \tag{59}$$

Further, once the auxiliary fluxes F_i are known, the convective terms that appear in the residuals defined in (28), (24), and (33) can be approximated as

$$\frac{\partial \rho u_i u_j}{\partial x_j}\simeq\frac{\delta_1 F_j \overline{u}_i^{1x_j}}{\delta_1 x_j}, \tag{60}$$

and

$$\rho u_j\frac{\partial T}{\partial x_j}\simeq\overline{F_j\frac{\delta_1 T}{\delta_1 x_j}}^{1x_j},\quad \rho u_j\frac{\partial Y_k}{\partial x_j}\simeq\overline{F_j\frac{\delta_1 Y_k}{\delta_1 x_j}}^{1x_j}, \tag{61}$$

respectively. Alternatively, the convective terms (24), (33) may also be discretized in the following way,

$$u_j\frac{\partial T}{\partial x_j}\simeq\overline{\bar{u}_j^{1x_j}\frac{\delta_1 T}{\delta_1 x_j}}^{1x_j},\quad u_j\frac{\partial Y_k}{\partial x_j}\simeq\overline{\bar{u}_j^{1x_j}\frac{\delta_1 Y_k}{\delta_1 x_j}}^{1x_j}. \tag{62}$$

Numerical experiments showed that the approximations given in (61) or (62) might be more stable than the other depending on the problem in hand; see Sections 4.1 and 4.2 for more details.

3.2.2. Fourth-order schemes

Herein we describe the fourth-order interpolation and differentiation techniques that are used to discretize the equations. Due to the similarity between the predictor and corrector stages of the time-marching method we will present the discretized forms of the equations appearing in the predictor step only. The fourth-order auxiliary fluxes and velocities are evaluated as

$$F_i^{*}=\frac{9}{8}\overline{\rho^{*}\tilde{u}_i}^{1x_i}-\frac{1}{8}\overline{\rho^{*}\tilde{u}_i}^{3x_i}-\Delta t\left(\frac{9}{8}\frac{\delta_1 p^{(1)*}}{\delta_1 x_i}-\frac{1}{8}\frac{\delta_3 p^{(1)*}}{\delta_3 x_i}\right) \tag{63}$$

and

$$u_i^{*}=\frac{1}{\rho^{*}}\left[\rho^{*}\tilde{u}_i-\Delta t\left(\frac{4}{3}\frac{\delta_2 p^{(1)*}}{\delta_2 x_i}-\frac{1}{3}\frac{\delta_4 p^{(1)*}}{\delta_4 x_i}\right)\right]. \tag{64}$$

respectively. The fourth-order spatial discretization for Eq. (31) is,

$$\frac{3\rho^{*}-4\rho^{n}+\rho^{n-1}}{2\Delta t}+\frac{9}{8}\frac{\delta_1 F_i^{*}}{\delta_1 x_i}-\frac{1}{8}\frac{\delta_3 F_i^{*}}{\delta_3 x_i}=0. \tag{65}$$

For the Poisson equation, the equivalent fourth-order spatial discretization of (29) is written as

$$\frac{3\rho^* - 4\rho^n + \rho^{n-1}}{2\Delta t} + \frac{9}{8}\frac{\delta_1}{\delta_1 x_i}\left(\frac{9}{8}\overline{\rho^*\tilde{u}_i}^{1x_i} - \frac{1}{8}\overline{\rho^*\tilde{u}_i}^{3x_i}\right) - \frac{1}{8}\frac{\delta_3}{\delta_3 x_i}\left(\frac{9}{8}\overline{\rho^*\tilde{u}_i}^{1x_i} - \frac{1}{8}\overline{\rho^*\tilde{u}_i}^{3x_i}\right) = \Delta t\left[\frac{9}{8}\frac{\delta_1}{\delta_1 x_i}\left(\frac{9}{8}\frac{\delta_1 p^{(1)*}}{\delta_1 x_i} - \frac{1}{8}\frac{\delta_3 p^{(1)*}}{\delta_3 x_i}\right) - \frac{1}{8}\frac{\delta_3}{\delta_3 x_i}\left(\frac{9}{8}\frac{\delta_1 p^{(1)*}}{\delta_1 x_i} - \frac{1}{8}\frac{\delta_3 p^{(1)*}}{\delta_3 x_i}\right)\right]. \tag{66}$$

Finally, the fourth-order approximations of the convective terms that appear in the residuals defined in (28), (24), and (33) are written as

$$\frac{\partial \rho u_i u_j}{\partial x_j} \simeq \frac{9}{8}\frac{\delta_1 F_j \overline{u}_i^{1x_j}}{\delta_1 x_j} - \frac{1}{8}\frac{\delta_3 F_j \overline{u}_i^{3x_j}}{\delta_3 x_j}, \tag{67}$$

$$u_j\frac{\partial T}{\partial x_j} \simeq \frac{4}{3}\overline{\bar{u}_j^{1x_j}\frac{\delta_1 T}{\delta_1 x_j}}^{1x_j} - \frac{1}{3}\overline{\bar{u}_j^{2x_j}\frac{\delta_2 T}{\delta_2 x_j}}^{2x_j} \tag{68}$$

and

$$u_j\frac{\partial Y_k}{\partial x_j} \simeq \frac{4}{3}\overline{\bar{u}_j^{1x_j}\frac{\delta_1 Y_k}{\delta_1 x_j}}^{1x_j} - \frac{1}{3}\overline{\bar{u}_j^{2x_j}\frac{\delta_2 Y_k}{\delta_2 x_j}}^{2x_j}, \tag{69}$$

respectively.

4. Numerical results

In this section, we present detailed results from two test problems that we considered in order to check the robustness and accuracy of the proposed algorithm. The first one is the large-eddy simulation of non-isothermal, turbulent channel flow. This is a case without chemical reactions but with strong temperature gradients due to the temperature difference between the two walls. The second test case is the flame–vortex interaction; this is a case of a laminar, unsteady reacting flow.

4.1. Large-eddy simulation of non-isothermal, turbulent channel flow

In this subsection, we consider turbulent flow in a channel whose walls are kept in different temperatures. This problem is treated numerically via LES. Let x, y and z, denote the streamwise, normal and spanwise directions, respectively. The dimensions of the domain are $4\pi\delta \times 2\delta \times \frac{4}{3}\pi\delta$, with δ being the channel half-width. The walls of the channel are normal to the y direction and are held at constant temperature. On the other hand, the boundaries of the domain normal to the x and z directions are periodic. Therefore, the total mass of the system is conserved, i.e., this is an example of flow in a closed domain. A mesh of 64^3 points is used. Uniform meshes are used in the streamwise and spanwise directions. A non-uniform mesh with hyperbolic tangent distribution is used in the wall-normal direction.

The dynamic subgrid-scale (SGS) model, Moin et al. [17] with the least square technique, Lilly [13] and averaging in the periodic directions is employed for the subgrid-scale terms. In the homogeneous directions, the convective terms of the momentum and energy equations are calculated using Eqs. (67) and (68), respectively. In the normal direction, Eq. (60) is used for the momentum equation and Eq. (62) for the energy equation. The fast Fourier transform is used in the periodic directions to solve the constant-coefficient pressure Poisson equation.

Let T_h and T_c denote the temperatures of the hot and cold walls, respectively. Three different cases, corresponding to different wall temperature ratios, are considered herein. More specifically, we have considered

ratios of $T_h/T_c = 1.01$, 2 and 8. For the cases of $T_h/T_c = 1.01$, 2 the initial fluid temperature was set at T_c. For the case $T_h/T_c = 8$ the initial condition was taken from previously calculated solutions with smaller wall-temperature ratios to shorten the required simulation time to reach stationary state. This strategy had been employed previously in Wang and Pletcher [29]. The simulation parameters are listed in Table 1. It is noted that in this section all parameters are defined using the dimensional quantities. However, unlike section (2) where a superscript $\hat{\cdot}$ denoted a dimensional variable, in this section the superscripts are dropped for the sake of clarity. Subscripts h and c denote the hot and cold wall, respectively. The subscript "w" is used for the values at the walls, w = {h, c}.

Table 1
Simulation parameters for the non-isothermal channel flow

T_h/T_c	Re_{cent}	$Re_{\tau h} - Re_{\tau c}$	$u_{\tau h}/\bar{u}_\tau - u_{\tau c}/\bar{u}_\tau$	B_{qh}	B_{qc}
1.01	3281	178.3–180.4	1.0–1.0	2.32×10^{-4}	2.33×10^{-4}
2.0	2521	91.2–224.1	1.13–0.86	1.35×10^{-2}	1.8×10^{-2}
8.0	1201	26.6–360.2	1.4–0.57	2.7×10^{-2}	7.2×10^{-2}

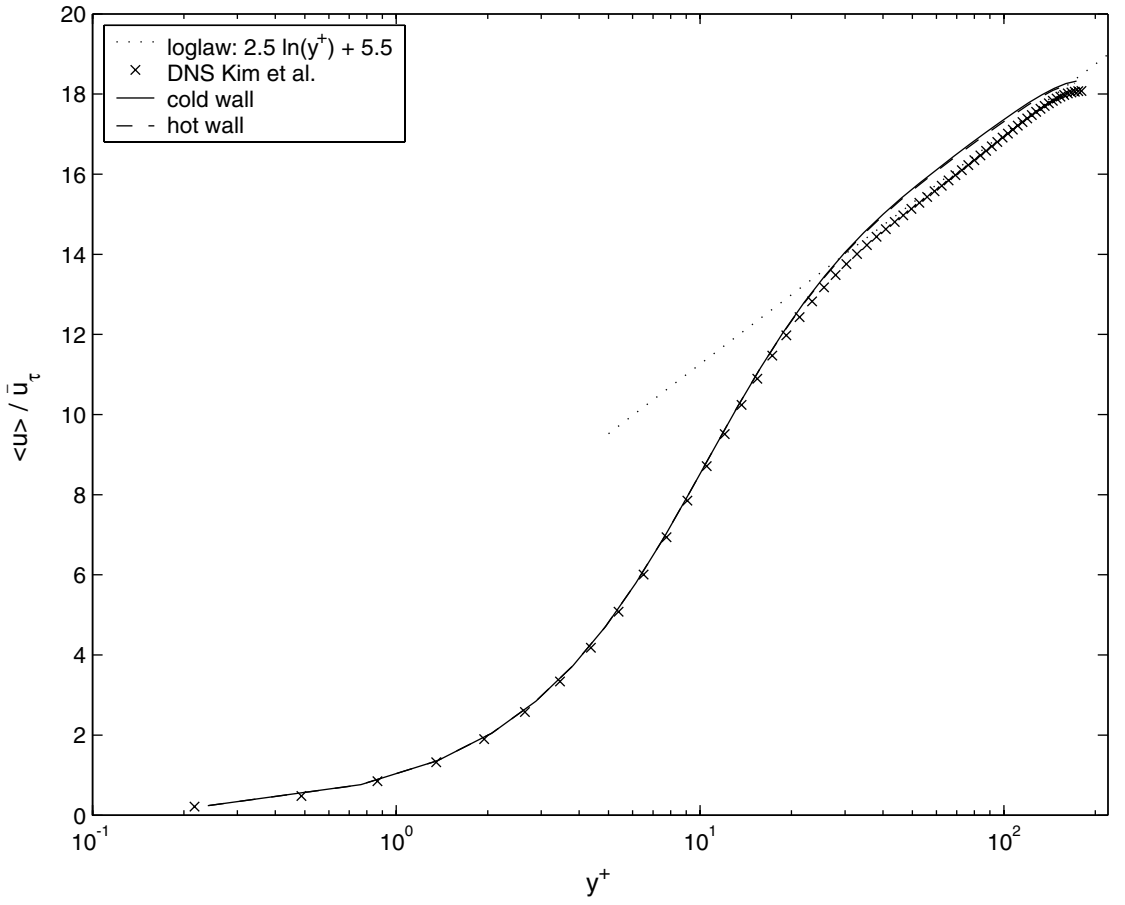

Fig. 1. Non-isothermal channel flow. Mean streamwise velocity profile $\langle u \rangle/\bar{u}_\tau$ in wall coordinates $y^+ = \rho_w \bar{u}_\tau y/\mu_w$ at $T_h/T_c = 1.01$ compared with the isothermal DNS of Kim et al. [11].

Also, $Re_{\text{cent}} = \rho_{\text{cent}} u_{\text{cent}} \delta / \mu_{\text{cent}}$ is the Reynolds number based on the values on the centerline. $Re_\tau = \rho_{\text{w}} u_\tau \delta / \mu_{\text{w}}$ is the Reynolds number based on the values near the wall. The friction velocity is $u_\tau = (\tau_{\text{w}}/\rho_{\text{w}})^{1/2}$, where τ_{w} is the wall shear stress and ρ_{w} is the density of the flow in the vicinity of the wall. The average friction velocity is $\bar{u}_\tau = (u_{\tau\text{h}} + u_{\tau\text{c}})/2$. B_q is the heat flux parameter defined as $B_q = q_{\text{w}}/(\rho_{\text{w}} c_p u_\tau T_{\text{w}})$, with q_{w} the heat flux and c_p the specific heat at constant pressure. A friction temperature T_τ is also defined as, $T_\tau = q_{\text{w}}/(\rho_{\text{w}} c_{\text{p}} u_\tau)$ and the average friction temperature is defined as, $\overline{T}_\tau = (T_{\tau\text{h}} + T_{\tau\text{c}})/2$.

The flow is driven by the same mean pressure gradient for all three temperature ratios. As a result, by increasing the temperature ratio, the centerline Reynolds number decreases, with a maximum of 3281 for the temperature ratio of 1.01, and a minimum of 1201 for the temperature ratio of 8. The difference between the friction Reynolds numbers of two walls increases with the temperature ratio. Thus, in order to have a well resolved flow near the wall, one has to pay attention to ensure that the distance of the first grid point away from the wall satisfies

$$y^+_{\text{f.p.}} \equiv \frac{\rho_{\text{w}} u_\tau y_{\text{f.p.}}}{\mu_{\text{w}}} < 1. \tag{70}$$

In the present calculations this condition was always satisfied.

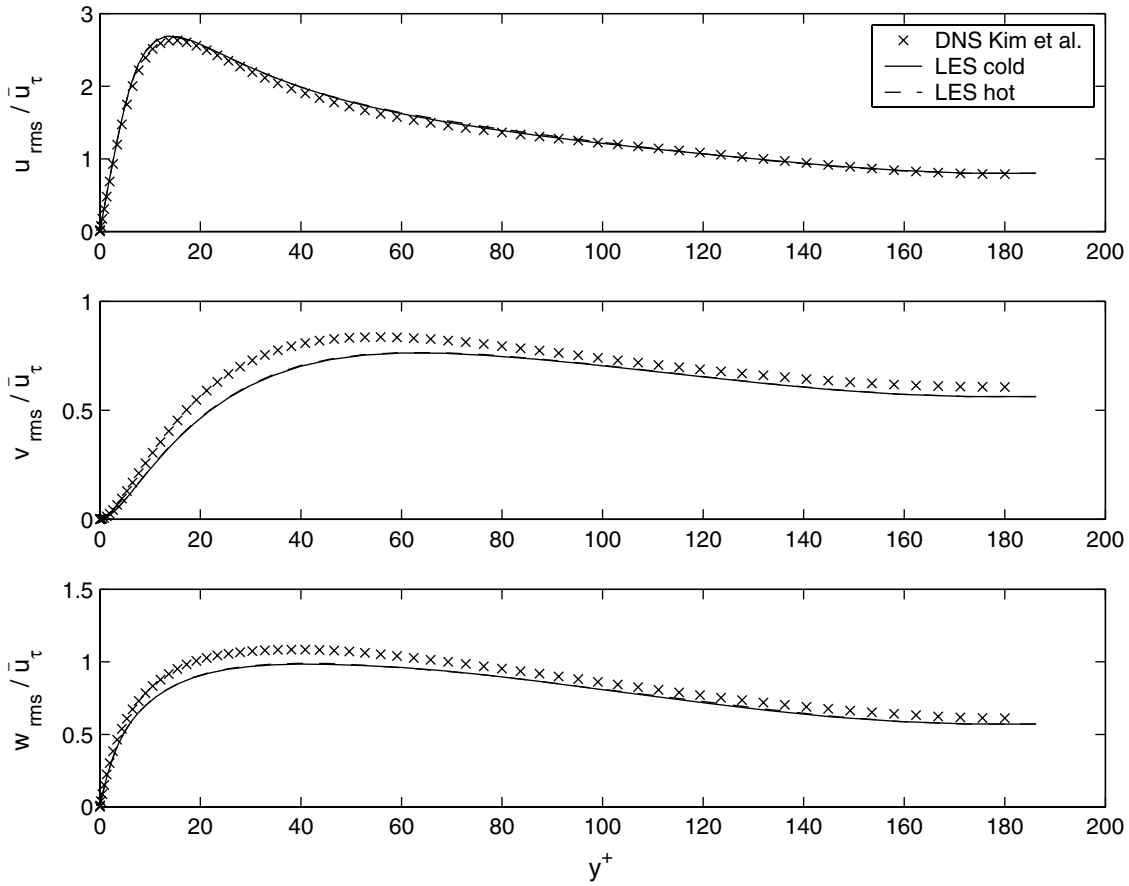

Fig. 2. Non-isothermal channel flow. Turbulence intensities ($u_{\text{rms}}/\bar{u}_\tau$, $v_{\text{rms}}/\bar{u}_\tau$, $w_{\text{rms}}/\bar{u}_\tau$) distributions in wall coordinates for the channel at $T_{\text{h}}/T_{\text{c}} = 1.01$ compared with the isothermal DNS of Kim et al. [11].

For comparison purposes between our results and the other LES and Direct Numerical Simulations (DNS) data, we used a molecular Prandtl number of 0.7 for the first case ($T_h/T_c = 1.01$) and a value of 0.8 for the other two cases ($T_h/T_c = 2$ and 8). In principle, the turbulent Prandtl number can be calculated using the dynamic procedure. During our numerical experiments, however, it was predicted that it remained almost constant from wall to wall for the cases we considered. Therefore, it was subsequently set to a constant value of $Pr_t = 0.9$ for the sake of computational savings.

As in earlier LES studies of non-isothermal channel flows, [22,29], buoyancy forces are neglected. This approximation is valid for values of the ratio Gr/Re^2 much smaller than unity, Gr being the Grashoff number of the problem. This ratio is directly proportional to the width of the channel. Therefore, buoyancy effects can be neglected for sufficiently small channel widths. For example, for the case of wall-temperature ratio equal to 8, $Re_{cent} = 1201$ and for channel width equal to 2 cm, then $Gr/Re^2_{cent} = 0.028$. LES studies on flows for which such effects are important certainly represent an interesting subject but they are beyond the scope of the present article.

Let $\langle\phi\rangle$ denote the time and space average of the instantaneous variable ϕ. Space averaging is performed in the homogeneous directions. The fluctuating part of the instantaneous variable ϕ is defined as $\phi' = \langle\phi\rangle - \phi$, with $\phi_{rms} = \langle\phi'\phi'\rangle^{1/2}$. The mean streamwise velocity profiles $\langle u\rangle/\bar{u}_\tau$ and the turbulence intensities

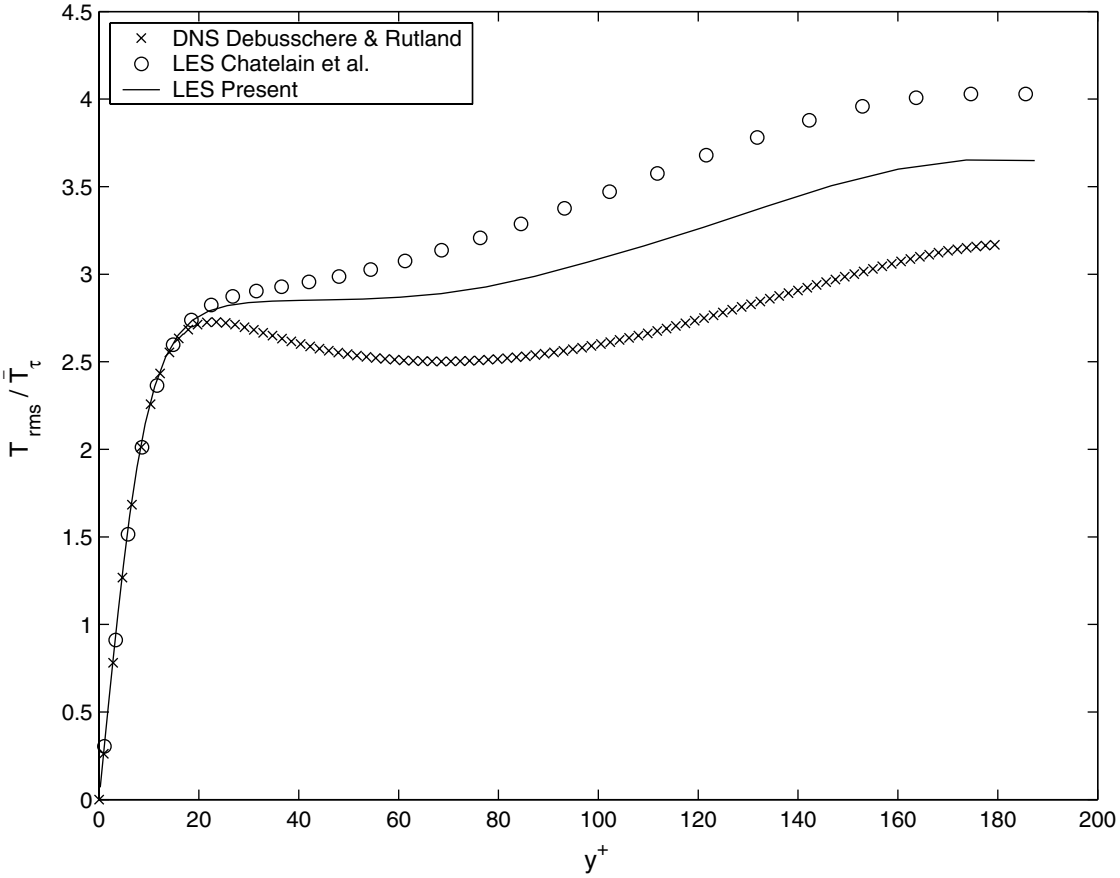

Fig. 3. Non-isothermal channel flow. Distribution $T_{rms}/\overline{T}_\tau$ for the channel flow at $T_h/T_c = 1.01$ in wall coordinates compared with the LES of Châtelain et al. [1] and DNS of Debusschere and Rutland [6].

($u_{\mathrm{rms}}/\bar{u}_\tau$, $v_{\mathrm{rms}}/\bar{u}_\tau$, $w_{\mathrm{rms}}/\bar{u}_\tau$) for $T_{\mathrm{h}}/T_{\mathrm{c}} = 1.01$ are shown in Figs. 1 and 2, respectively, as functions of the wall coordinates $y^+ = \rho_{\mathrm{w}}\bar{u}_\tau y/\mu_{\mathrm{w}}$. In Fig. 1, the logarithmic law of the wall, $u^+ = 2.5\ln y^+ + 5.5$, is also plotted for comparison. The results are compared with the DNS data of Kim et al. [11]. The agreement between those DNS data and our LES results is very good. For this small temperature ratio, the temperature difference has almost no effect on the properties of the fluid and the graphs of hot and cold sides collapse onto a single graph. Accordingly, for the other graphs of this case we will only show the cold side distributions.

In Fig. 3, we compare our LES results for the temperature fluctuation distribution $T_{\mathrm{rms}}/\overline{T}_\tau$ with the DNS data of Debusschere and Rutland [6] and the LES results of Châtelain et al. [1]. It can be observed that there are discrepancies between LES and DNS data at large values of y^+. However, the discrepancy of our LES results with respect to the DNS data is smaller than the discrepancy of the LES results in [1].

In [1], the authors proposed upwinding the convective terms in the energy equation to have a better agreement between the DNS and LES data. However, they also mentioned that upwinding leads to an under-prediction of the temperature–velocity correlation $\langle u'T'\rangle/(\bar{u}_\tau\overline{T}_\tau)$ and also the temperature fluctuations non-dimensionalized by the walls temperature difference, $T_{\mathrm{rms}}/\Delta T$, (Figs. 19 and 20 in [1]). For this reason, we opted to maintain central differencing of the convective terms in the energy equation in our algorithm.

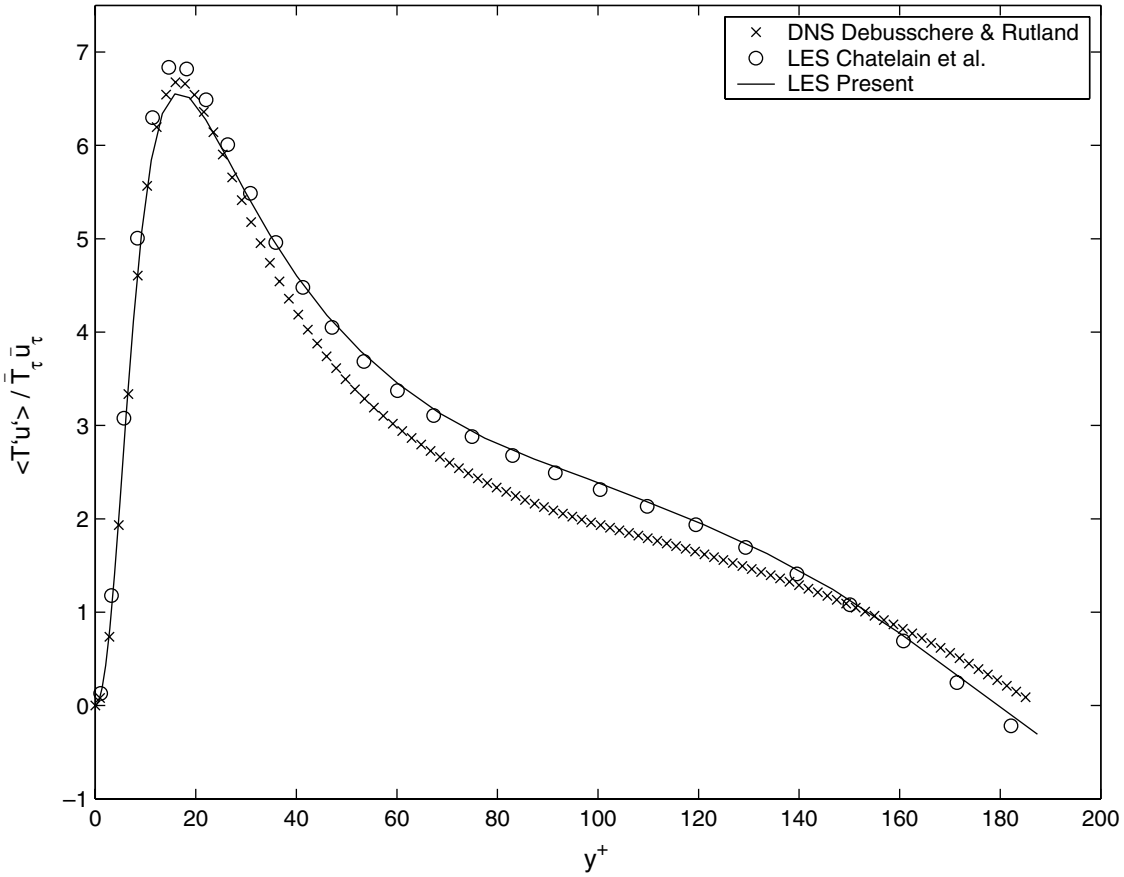

Fig. 4. Non-isothermal channel flow. Distribution of $\langle T'u'\rangle/\overline{T}_\tau\bar{u}_\tau$ for the channel at $T_{\mathrm{h}}/T_{\mathrm{c}} = 1.01$ in wall coordinates compared with the LES of Châtelain et al. [1] and the DNS of Debusschere and Rutland [6].

The Nusselt number, defined as

$$Nu = \frac{4\delta(\partial T/\partial y)_{\mathrm{w}}}{T_{\mathrm{w}} - T_{\mathrm{b}}}, \tag{71}$$

with T_{b} the bulk temperature, is equal to 23.6 in the present study. This compares well to the Nusselt number values of 23.3 and 24.3 that were reported in [1,6], respectively. The bulk temperature T_{b}, is defined using the bulk density ρ_{b} and velocity U_{b}

$$\rho_{\mathrm{b}} = \frac{1}{2\delta}\int_{-\delta}^{\delta}\rho\,\mathrm{d}y, \quad U_{\mathrm{b}} = \frac{1}{2\delta\rho_{\mathrm{b}}}\int_{-\delta}^{\delta}\rho u\,\mathrm{d}y, \quad T_{\mathrm{b}} = \frac{1}{2\delta\rho_{\mathrm{b}}U_{\mathrm{b}}}\int_{-\delta}^{\delta}\rho uT\,\mathrm{d}y. \tag{72}$$

The temperature–velocity correlation $\langle T'u'\rangle/(\overline{T}_\tau\bar{u}_\tau)$ and mean temperature profile $\langle T\rangle/\overline{T}_\tau$ are reported in Fig. 4 and 5. For these two graphs, there is a good agreement between the DNS and LES data.

Fig. 6 shows the mean velocity profiles $\langle u^+_{\mathrm{VD}}\rangle/u_{\tau\mathrm{c}}$ in wall coordinates for the cold wall region for three different temperature ratios. Fig. 7 shows the same graphs for the hot wall region. In these figures, the van Driest velocity transformation, van Driest [7], was employed to collapse the results of a variable density flow into the classical logarithmic law. This transformation is expressed as

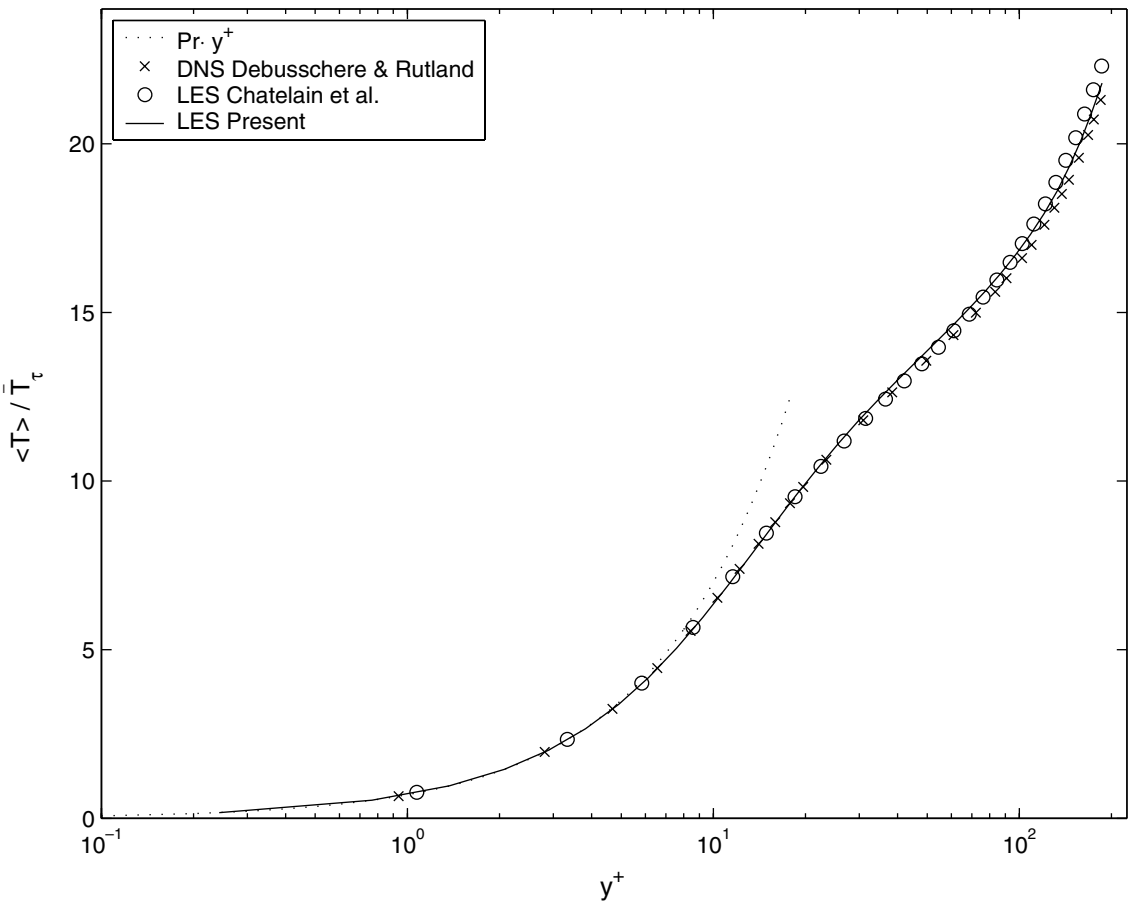

Fig. 5. Non-isothermal channel flow. Mean temperature profile $\langle T\rangle/\overline{T}_\tau$ for the channel at $T_{\mathrm{h}}/T_{\mathrm{c}} = 1.01$ in wall coordinates compared with the LES of Châtelain et al. [1] and DNS of Debusschere and Rutland [6].

$$u^+_{\mathrm{VD}} = \int_0^{u^+} \left(\frac{\rho}{\rho_{\mathrm{w}}}\right)^{1/2} \mathrm{d}u^+. \tag{73}$$

In Fig. 6, we can observe a significant deviation of the velocity profiles from the reference empirical law of the wall for the case of temperature ratio of 8, at the side of the cold wall. On the other hand, no such deviation is observed at the side of the hot wall, Fig. 7. The same over-prediction at the cold wall side was reported in [29] for a temperature ratio of 3. This deviation may be attributed to the fact that the van Driest transformation does not provide an effective means for collapsing results of variable density flows if the temperatures (density) variations are too high. On the other hand, the result reported in [22] for a temperature ratio of 4 showed good agreement with the logarithmic law by use of the van Driest transformation. In [22], however, the dimensionless thermal conductivity and dynamic viscosity were chosen to be proportional to $1/\sqrt{T}$ instead of following Sutherland law. Such dependence of the transport coefficients on the temperature is non-physical.

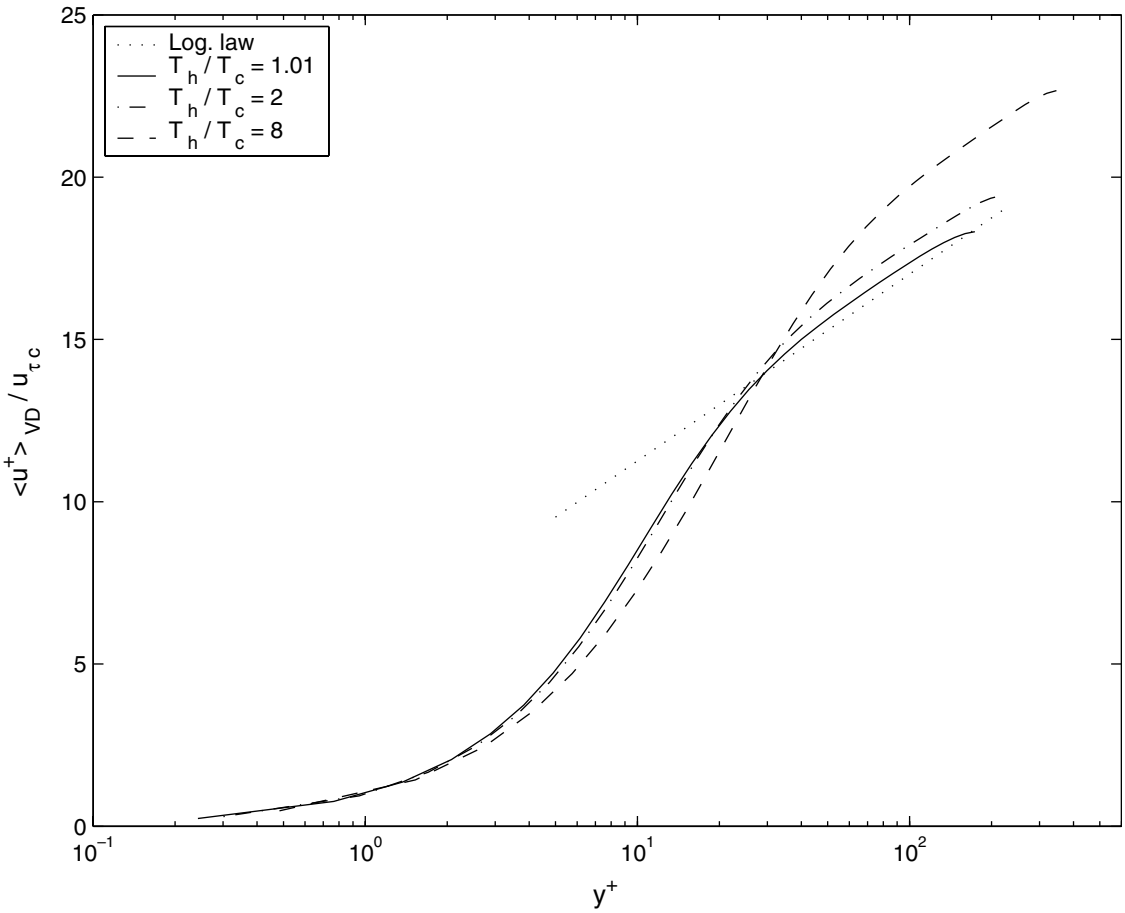

Fig. 6. Non-isothermal channel flow. Mean velocity profiles $\langle u^+_{\mathrm{VD}}\rangle/u_{\tau c}$ for the cold wall region in wall coordinates $y^+ = \rho_{\mathrm{wc}} u_{\tau c} y/\mu_{\mathrm{wc}}$, at three different temperature ratios: $T_{\mathrm{h}}/T_{\mathrm{c}} = 1.01$, 2 and 8.

And finally, in Figs. 8–10 we present results of the turbulence kinetic energy,

$$k_{\mathrm{t}} = \frac{1}{2}\frac{\langle u_i' u_i' \rangle}{\bar{u}_\tau^2}, \tag{74}$$

the temperature fluctuations normalized by the wall temperature difference and the mean temperature distribution across the channel, respectively. We note that the fully developed condition requires that the wall heat flux be the same on both walls. According to the Sutherland law, the thermal conductivity increases with the temperature, which results in a steeper temperature gradient on the cold wall than on the hot wall. This behaviour can be clearly seen in Fig. 10. The turbulence kinetic energy is also smaller for higher temperature ratios. This can be contributed to the decrease of the bulk Reynolds numbers in higher temperature ratios for a fixed pressure gradient.

4.2. Flame–vortex interaction

In this subsection, we present simulations of the 2D problem of the interaction of a vortex pair with a laminar premixed flame. This test case has been studied by many authors in the past (see [3,19–21,25] and

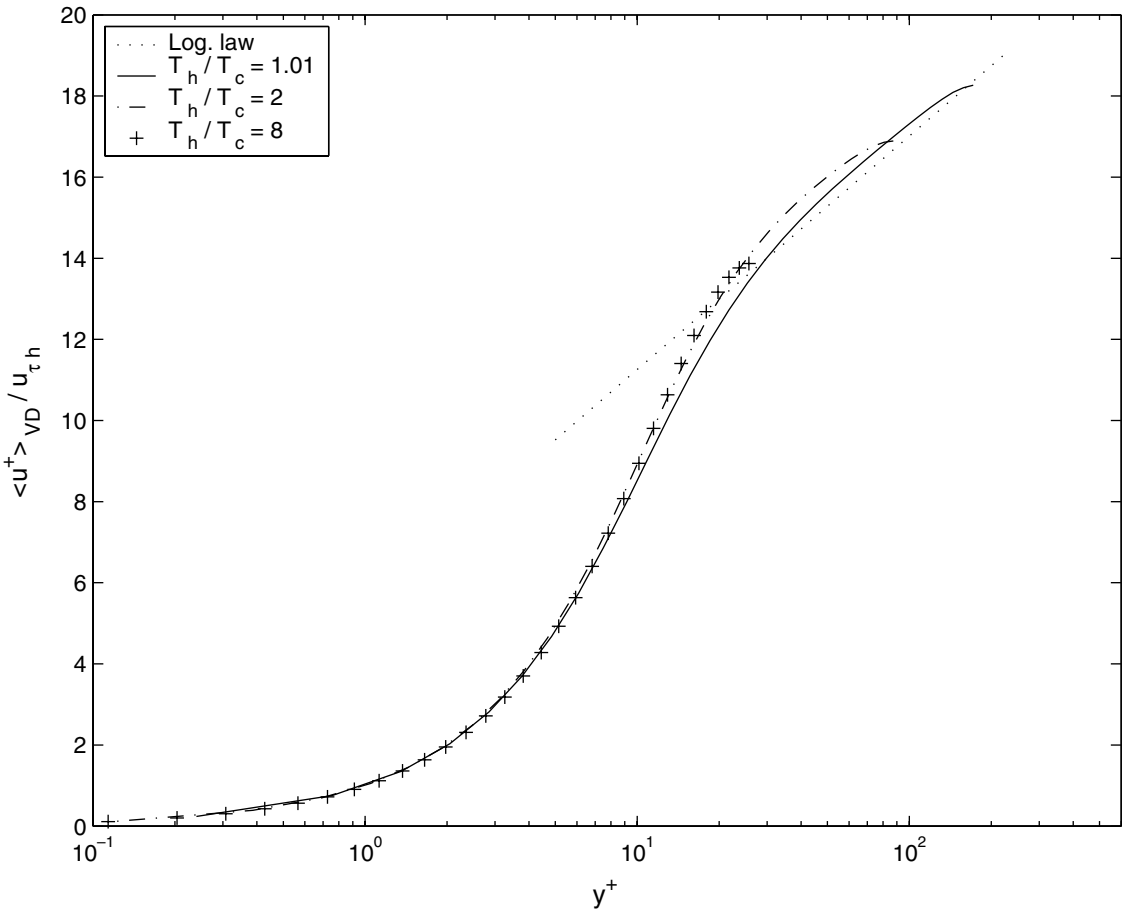

Fig. 7. Non-isothermal channel flow. Mean velocity profiles $\langle u_{\mathrm{VD}}^+ \rangle / u_{\tau \mathrm{h}}$ for the hot wall region in wall coordinates $y^+ = \rho_{\mathrm{wh}} u_{\tau \mathrm{h}} y / \mu_{\mathrm{wh}}$, at three different temperature ratios. $T_{\mathrm{h}}/T_{\mathrm{c}} = 1.01$, 2 and 8.

references therein) and serves us as a useful test case to assess the stability of the present algorithm in flows with chemical reactions and in flows in open domains. The chemistry model is a simple, single-step, irreversible reaction represented by

$$R(\text{Reactants}) \rightarrow P(\text{Products}) \tag{75}$$

and governed by Arrhenius kinetics. Let S_L denote the laminar flame speed and α the heat diffusivity in the fresh gas. The reference length of this problem is defined as $L_{\text{ref}} = \alpha/S_L$. The reference velocity is set equal to the laminar flame speed, $u_{\text{ref}} = S_L$. Then, the reference time is $t_{\text{ref}} = L_{\text{ref}}/u_{\text{ref}}$. The temperature, density and fuel mass fraction in the fresh gas are used as the reference values for these quantities. Non-dimensionalization of all variables has been made with respect to these reference values.

The nondimensional form of the Arrhenius kinetics law is given by

$$\dot{w}_R = t_{\text{ref}} B \rho Y_R \exp(-T_a/T), \tag{76}$$

where T_a is the activation temperature and B is the pre-exponential constant that sets the chemical time scale. The simulation parameters of the laminar premixed flame and the reference values used in Eq.

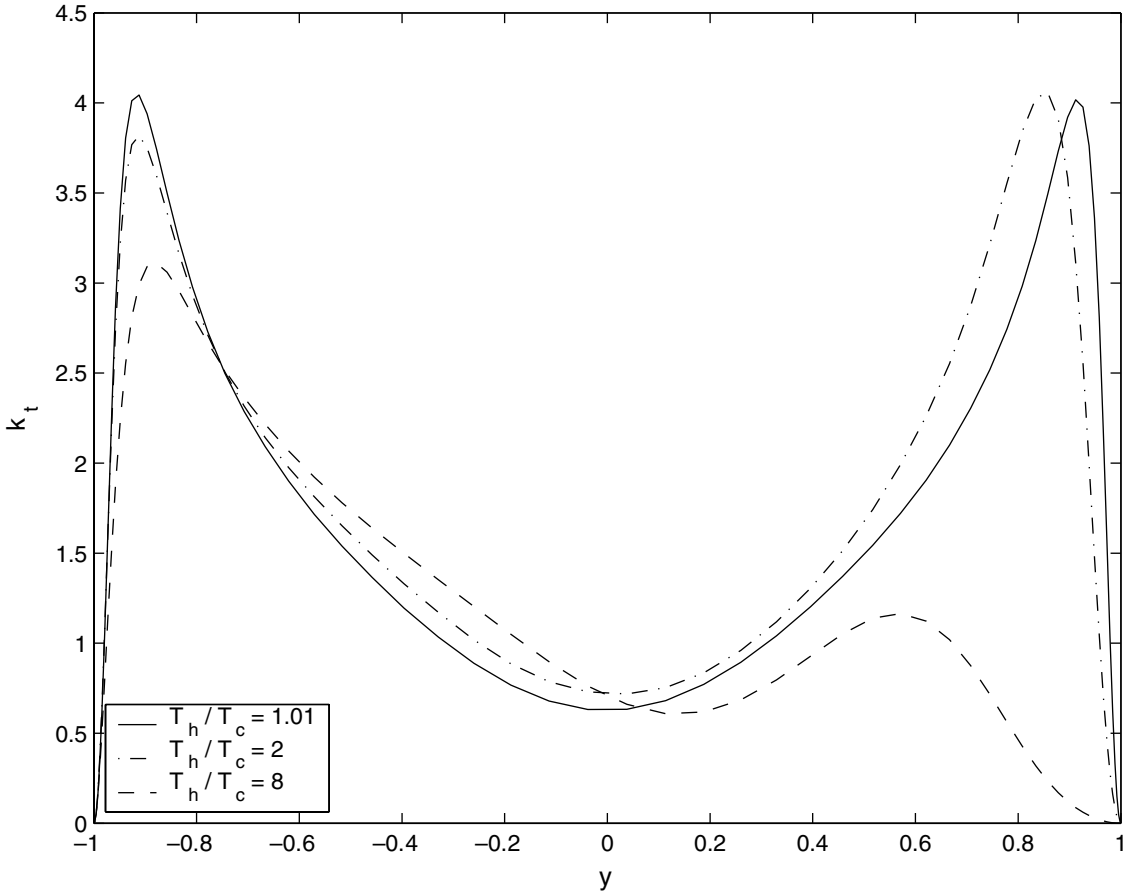

Fig. 8. Non-isothermal channel flow. Turbulence kinetic energy $k_t = 0.5\langle u_i' u_i' \rangle / \bar{u}_\tau^2$, distribution across the channel at three different temperature ratios. $T_h/T_c = 1.01$, 2 and 8.

(76) are given in Table 2. The parameters are chosen in a way that that the laminar flame approximates the stoichiometric methane/air flame at normal conditions.

The first step of the simulation is to calculate the profile of a steady, one-dimensional laminar premixed flame. In this study, the proposed algorithm has been used to generate this profile as the steady-state solution of the initial-value problem of a discontinuous profile consisting of two different uniform states. The profiles for the density, fuel mass fraction and temperature across the flame, as computed with the proposed algorithm, are plotted in Fig. 11. It can be observed that the temperature jump across the flame is $T_b/T_u = 7.4$, with T_b and T_u the temperatures of the burnt and unburnt gases, respectively. This value is close to the adiabatic flame temperature of stoichiometric combustion of methane/air at normal conditions.

The flame thickness δ_L^0 defined as, see Poinsot and Veynante [24],

$$\delta_L^0 = \frac{T_b - T_u}{\max(|\frac{\partial T}{\partial x}|)}. \tag{77}$$

For the flame under consideration, the (dimensional) flame thickness is equal to $\delta_L^0 = 0.33$ (mm). Another thickness, called the total thickness δ_L^t, defined as the distance over which the reduced temperature $\theta = (T - T_u)/(T_b - T_u)$ changes from 0.01 to 0.99. In this case, its value is $\delta_L^t = 0.81$ (mm).

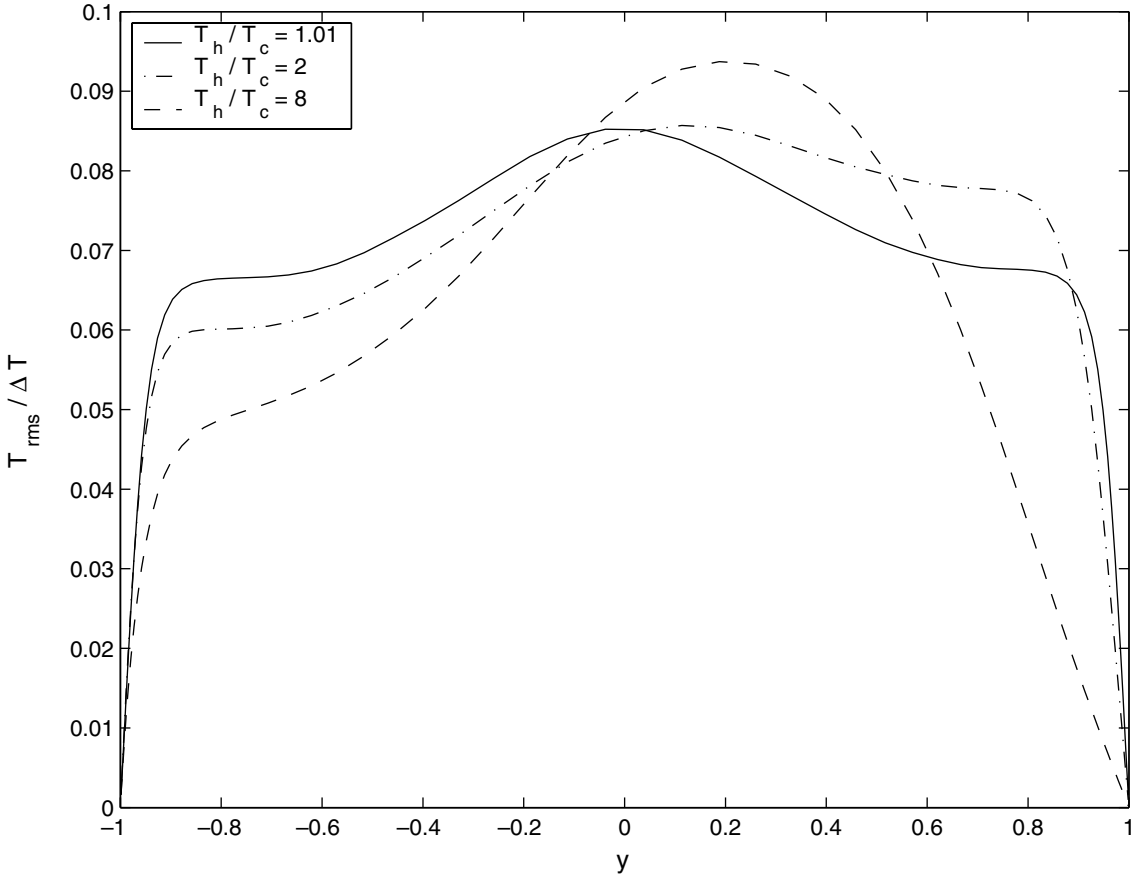

Fig. 9. Non-isothermal channel flow. Distribution of $T_{rms}/\Delta T$ across the channel at three different temperature ratios. $T_h/T_c = 1.01$, 2 and 8.

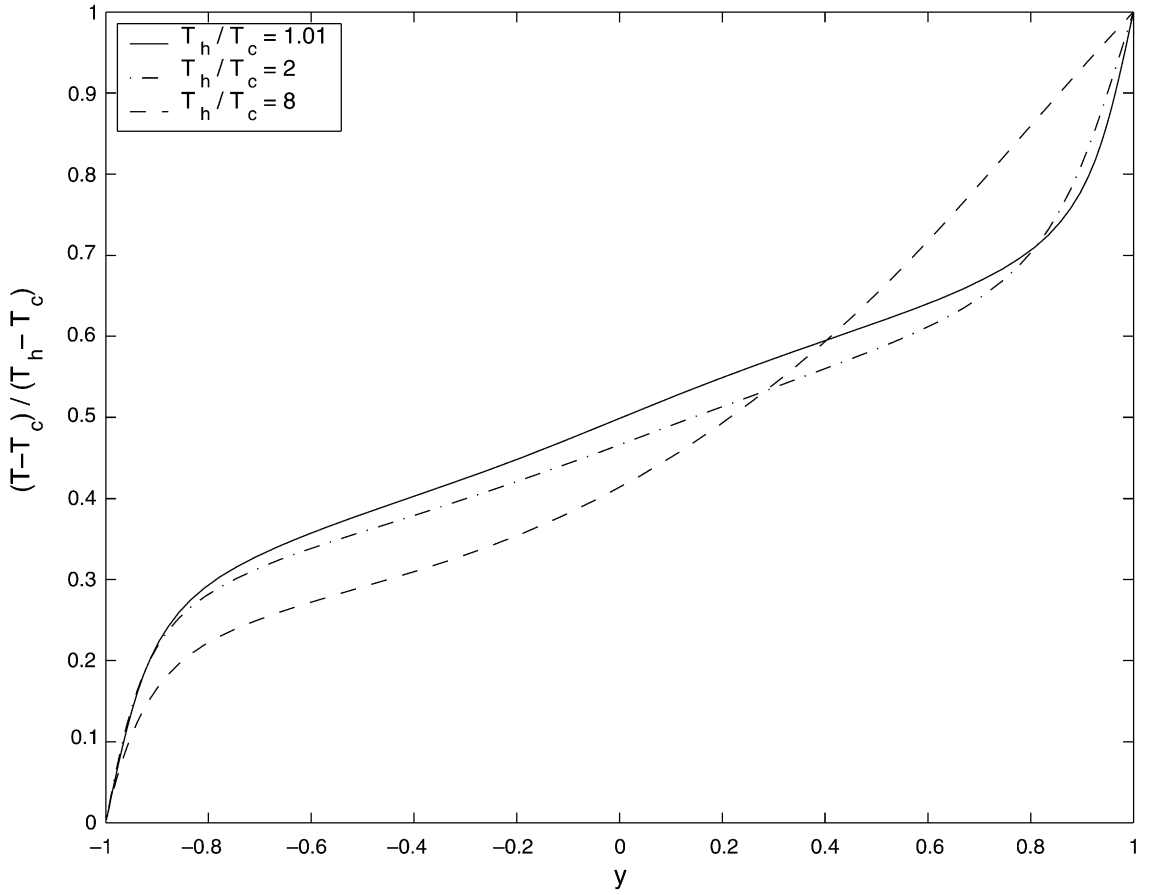

Fig. 10. Non-isothermal channel flow. Distribution of normalized temperature, $(T - T_c)/(T_h - T_c)$, across the channel at three different temperature ratios. $T_h/T_c = 1.01$, 2 and 8.

Table 2
Simulation parameters for the premixed laminar flame

L_{ref} (m)	u_{ref} (m/s)	B (1/s)	T_a	Δh_R^0	Pr	Re
5.45×10^{-5}	0.416	7×10^6	30	6.4	0.7	1.43

L_{ref}, u_{ref} and B are dimensional. T_a and Δh_R^0 are normalized by the reference quantities. $Re = u_{ref} L_{ref}/\nu$.

The initial condition for the flame–vortex interaction problem consists of the superposition of the initial profile and the field generated by system of two counter-rotating vortices on the upstream side of the flame front. If u and v denote the velocities in the x and y directions, the velocity field of a vortex located at x_0 and y_0 is defined as

$$u = \frac{C(y - y_0)}{R^2} \exp(-r^2/2), \quad v = -\frac{C(x - x_0)}{R^2} \exp(-r^2/2), \tag{78}$$

with $r = \sqrt{((x - x_0)^2 + (y - y_0)^2)}/R$. Also, in the equation above, C and R represent the vortex strength and vortex radius, respectively. In our case, we have used the following values: $C = \pm 70$ and $R = 4$. The

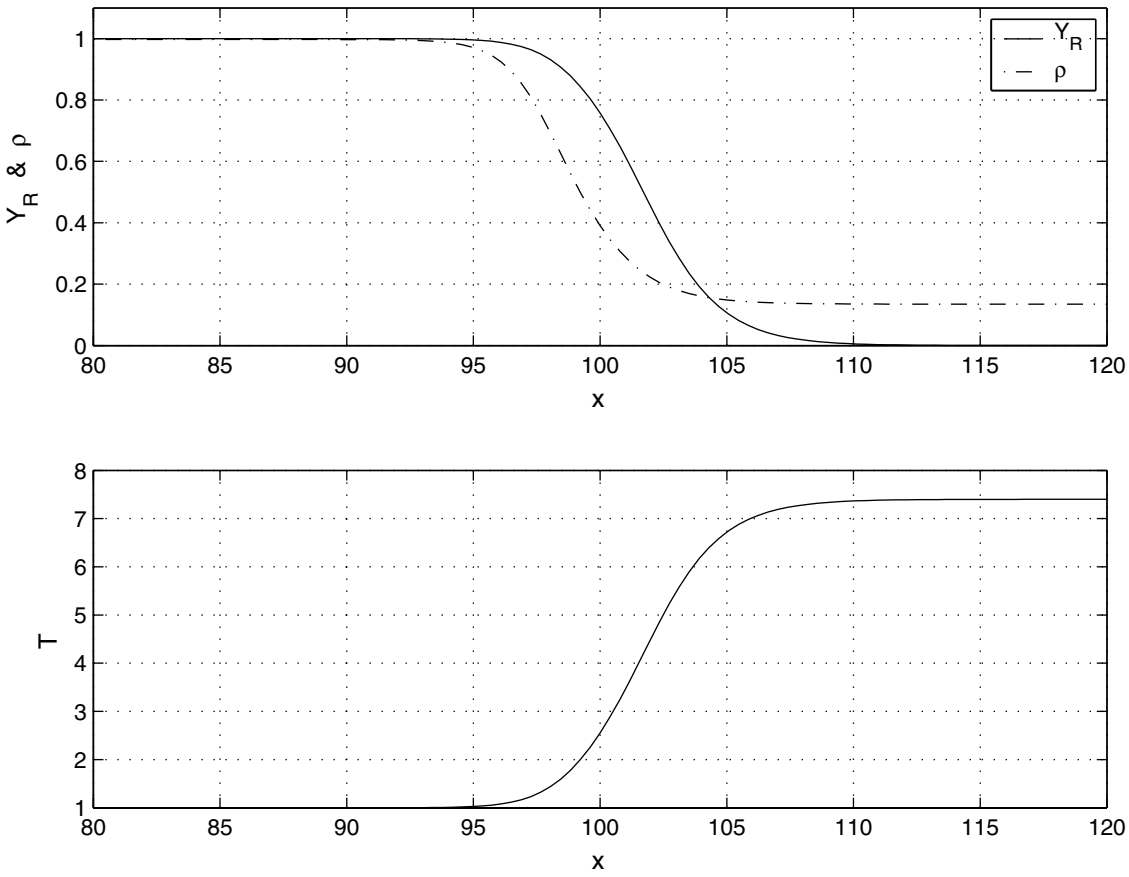

Fig. 11. 1D premixed flame. Initial profiles for the fuel mass fraction Y_R, density ρ and temperature T.

initial locations of the clockwise and counterclockwise rotating vortices are at ($x_0 = 37.5$, $y_0 = 75$) and ($x_0 = 62.5$, $y_0 = 75$), respectively. The maximum rotational velocity of the initial vortices is 10.6, but as they approach the flame, they loose their strength due to the fluid viscosity and the interaction with the flame.

A rectangular domain of size $L_x = 100$ and $L_y = 200$ is considered. The flame front is initially located in the middle of the domain at $L_y/2$ along the x direction. Periodic conditions are applied on the boundaries normal to the y direction. Inflow boundary conditions (constant flow variables) are applied along $y = 0$ and outflow boundary conditions (zero normal derivatives) are applied along $y = L_y$. In other words, this is a case of a flow in an open domain. The spatial derivatives are discretized with the second-order method described in Section 3.2.1. The convective terms of the momentum, energy and species equations are calculated using Eqs. (60) and (61), respectively. The fast Fourier transform is used in the periodic direction to solve the constant-coefficient pressure Poisson equation.

The flow field is computed on three different regular grids; namely, 64×128, 128×256 and 256×512 points. Fig. 12 shows four instantaneous contour fields of temperature and vorticity on the finest grid. The time span is from $t = 10$ to 25 with a time interval of 5. In Fig. 12(a), the vortices are still far from the flame front. Consequently, the front is not yet affected by the presence of the vortices. As the vortices

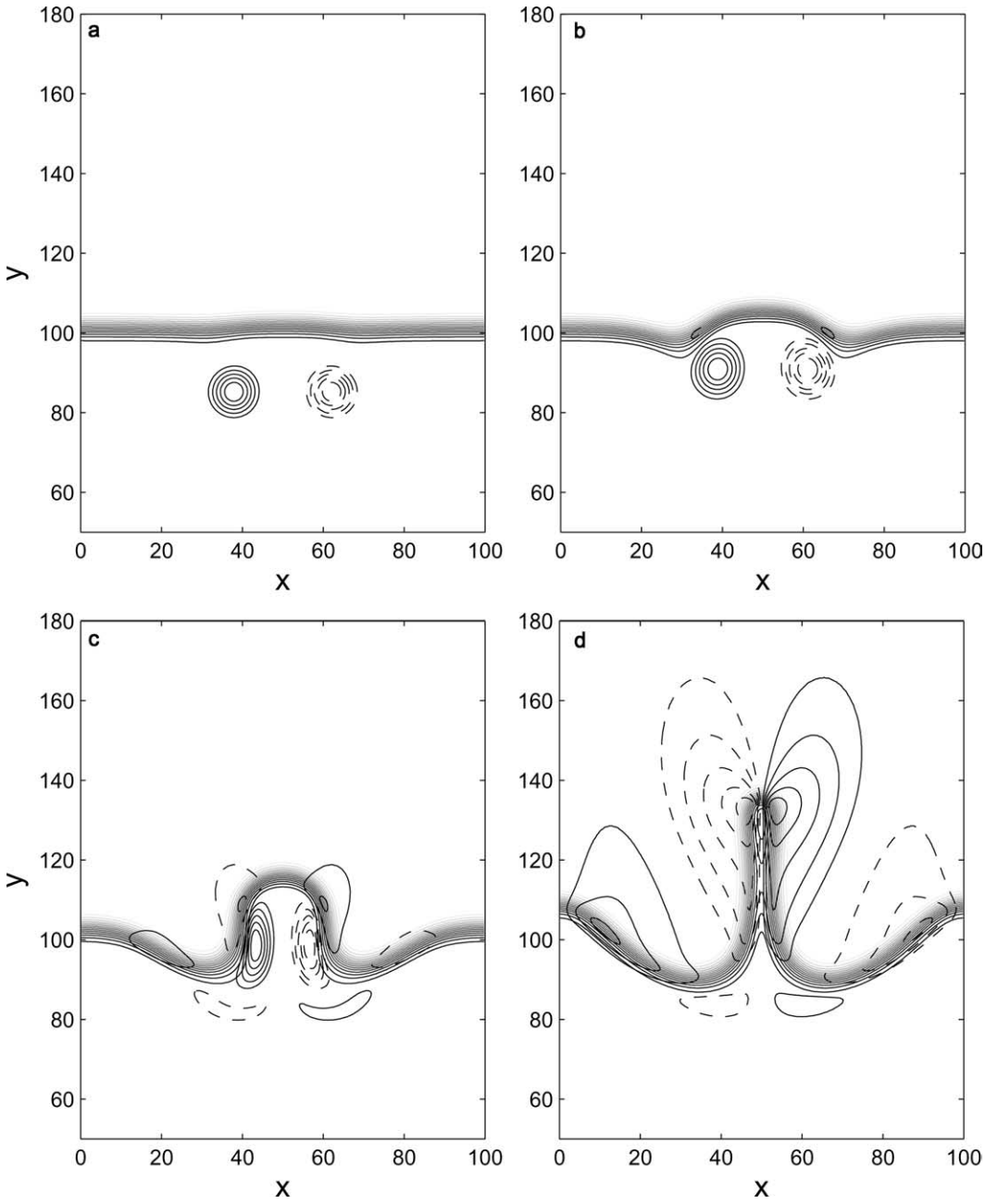

Fig. 12. Flame–vortex interaction. Instantaneous contour fields of temperature and vorticity. (a) $t = 10$, (b) $t = 15$, (c) $t = 20$, (d) $t = 25$. Bold (—) and dashed (– –) lines correspond to positive (counterclockwise rotation) and negative (clockwise rotation) vorticities, respectively.

come closer to the flame, Fig. 12(b), they begin to stretch the reaction zone and the geometry of the flame becomes distorted due to the local compressive tangential strain. Further, the flame thickness is increased at the two curved "cusp" locations. As mentioned, among other, in [21], the dependence of the flame thickness

on stretch is a result of the convective strain field acting on the flame. When the vortices interact further with the flame, Fig. 12(c), flame-generated vorticity starts to appear in the product gas above the flame front, Mueller et al. [19]. In Fig. 12(d), the flame generated vorticity is convected and diffused away from the flame front. The shape of the initial vortices is thus elongated in the y direction.

The figures mentioned above confirm that the shape of the reaction zone (stretched by the vortex pair) and the deformation of the vortices are very similar to the ones reported in previous studies; see, for example [3,19,21]. Quantitative comparisons between our results and these earlier ones cannot be made because in the earlier works the authors have either considered detailed reaction mechanisms and/or they have not provided sufficient information to reproduce the initial profile of the laminar flame.

Profiles of the density, velocity in the y direction and fuel mass fraction along the centerline at $t = 25$ for the three different resolutions are shown in Fig. 13. Finally, the time evolution of the total reaction rate for the different grid resolutions is shown in Fig. 14. The total reaction rate increases in time because of increased flame surface that results from the interaction of the flame with the vortices. Plots of this rate, but for flames with different reaction parameters, have been previously presented in [3]. Nonetheless, our predictions for its growth in time is very similar to the prediction in [3]. Finally, it is important to mention

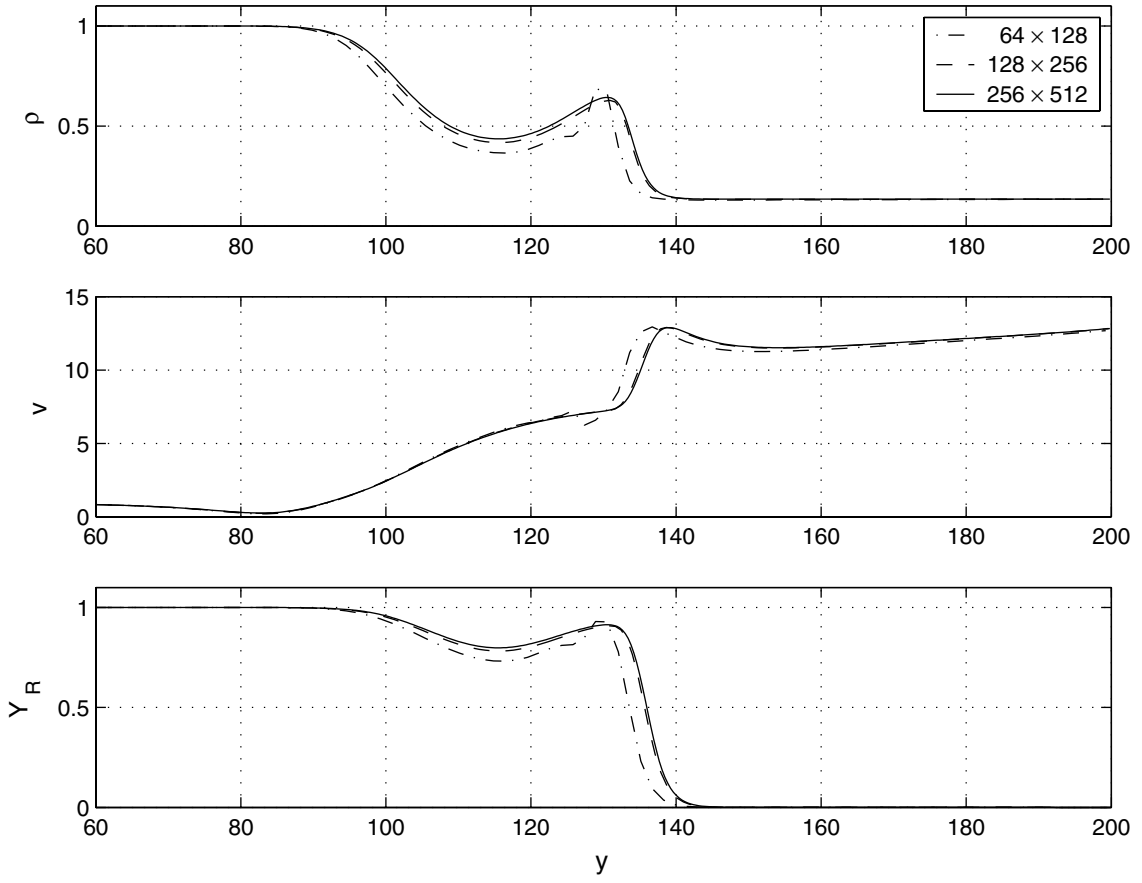

Fig. 13. Flame–vortex interaction. Variations of the density ρ, velocity in the y direction v and fuel mass fraction Y_R for three different resolutions, along the centerline $x = L_x/2$, at $t = 25$. Dot-dashed (– · –) ($ni = 64$, $nj = 128$), dashed (– –) ($ni = 128$, $nj = 256$), and bold (—) ($ni = 256$, $nj = 512$).

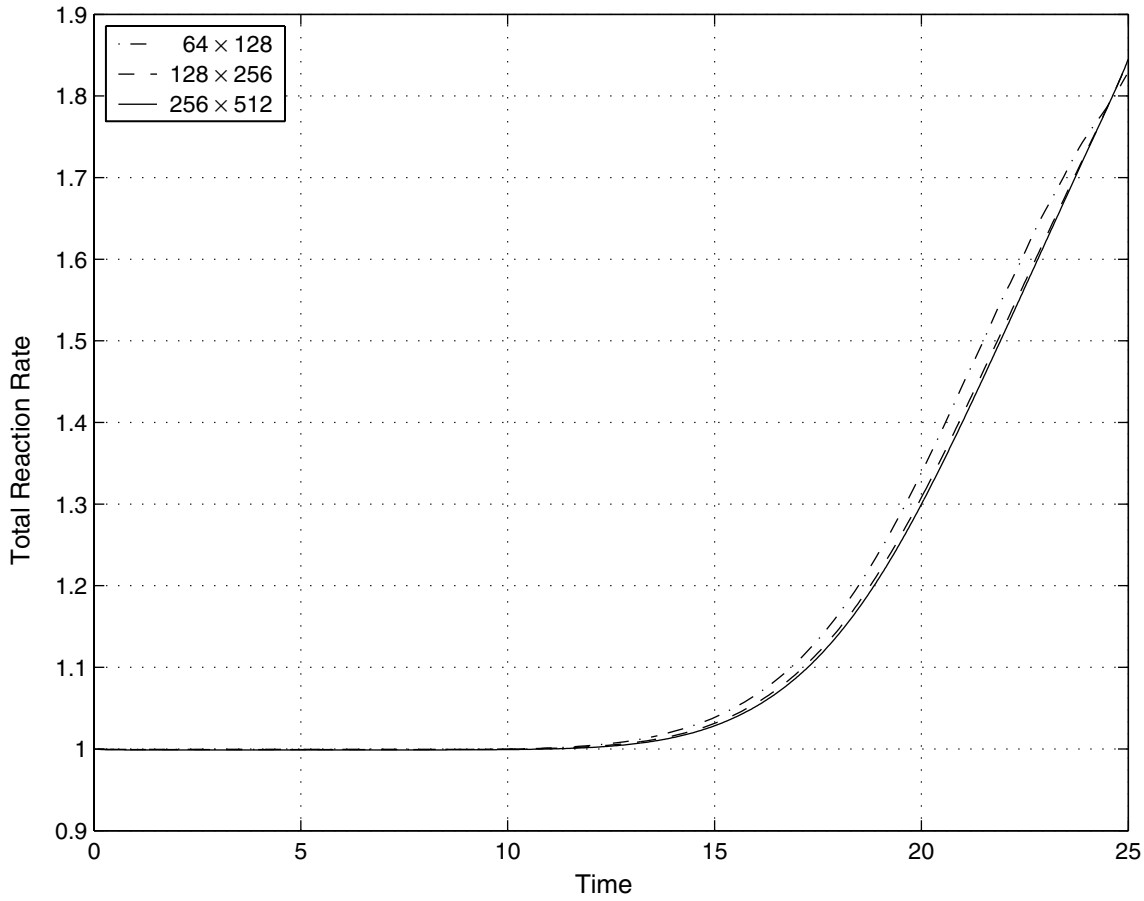

Fig. 14. Flame–vortex interaction. Time evolution of the total reaction rate, for three different resolutions (see caption of Fig. 13 for details).

that the results obtained with three different resolutions, Figs. 13 and 14 confirm that numerical convergence is in fact obtained by successive refinement of the grid refinement. In particular, it can be observed in these plots that the differences in the numerical results from two successive resolutions are getting smaller as the grid is refined.

5. Conclusions

In this article, a new algorithm for time-accurate calculations of low Mach number, variable density flows has been presented. This algorithm can be applied to both open and closed domains. It is based on a two-stage predictor–corrector method. This algorithm is particularly useful for unsteady flows with strong temperature gradients and for reacting flows. A constant-coefficient Poisson equation, which is computationally more efficient than the variable-coefficient one, is solved for the pressure. In the past, the approximation of the time derivative of the density field in the pressure Poisson equation has been identified as a destabilizing factor of the algorithms. However, in the numerical simulations performed with the

proposed algorithm no such stability problems were observed. For spatial discretization we opted for a collocated grid and not a staggered one because collocated grids offer computational simplicity and straightforward extension to curvilinear coordinate systems. The odd–even decoupling problem that is typically encountered in collocated grids is avoided by using a flux interpolation technique.

The robustness and accuracy of the algorithm have been assessed through simulations of two well-known test problems; the turbulent channel flow with temperature gradients and the flame–vortex interaction problem. The results obtained with the proposed algorithm are in very good agreement with the ones reported in earlier studies. Additionally, the proposed algorithm is robust enough to efficiently handle cases with strong temperature and density gradients. Results for such cases had not yet been available in the literature.

Acknowledgments

We thank Dr. Habib N. Najm at Sandia National Laboratories for helpful discussions, and also Mr. Alexandre Châtelain at INPG, Grenoble, France, and Mr. Nicolas de Champvallins at ENSTA, Paris, France, for providing us with the LES and DNS data that we used in our channel flow comparisons.

References

[1] A. Châtelain, F. Ducros, O. Métais, Large-eddy simulation of turbulent heat transfer: proper convection numerical schemes for temperature transport, Int. J. Numer. Meth. Fluids 44 (2004) 1017.
[2] A.J. Chorin, A numerical method for solving incompressible viscous flow problems, J. Comput. Phys. 2 (1967) 12.
[3] O. Colin, F. Ducros, D. Veynante, T. Poinsot, A thickened flame model for large-eddy simulations of turbulent premixed combustion, Phys. Fluids 12 (2000) 1843.
[4] A.W. Cook, J.J. Riley, Direct numerical simulation of a turbulent reactive plume on a parallel computer, J. Comput. Phys. 129 (1996) 263.
[5] J. de Charentenay, D. Thévenin, B. Zamuner, Comparison of direct numerical simulations of turbulent flames using compressible or low mach number formulations, Int. J. Num. Meth. Fluids 39 (2002) 497.
[6] B. Debusschere, C.J. Rutland, Turbulent scalar transport mechanisms in plane channel and couette flows, Int. J. Heat Mass Transfer 47 (2004) 1771.
[7] E.R. van Driest, Turbulent boundary layer in compressible fluids, J. Aeronaut. Sci. 18 (3) (1951) 145.
[8] M. Germano, U. Piomelli, P. Moin, W.H. Cabot, A dynamic subgrid-scale eddy viscosity model, Phys. Fluids A 3 (1991) 1760.
[9] Y. Hou, K. Mahesh, A robust, colocated, implicit algorithm for direct numerical simulation of compressible, turbulent flows, J. Comput. Phys. 205 (2005) 205–221.
[10] A. Jameson, Time dependent calculations using multigrid, with applications to unsteady flows past airfoils and wings, AIAA paper, 91-1596, 1991
[11] J. Kim, P. Moin, R. Moser, Turbulence statistics in fully developed channel flow at low reynolds number, J. Fluid Mech. 177 (1987) 133.
[12] B. Lessani, J. Ramboer, C. Lacor, Efficient large-eddy simulations of low mach number flows using preconditioning and multigrid, Int. J. Comput. Fluid Dynamics 18 (2004) 221.
[13] D. Lilly, A proposed modification of the germano subgrid-scale closure method, Phys. Fluids A 4 (1992) 633.
[14] A. Majda, J. Sethian, The derivation and numerical solution of the equations for zero mach number combustion, Combust. Sci. Technol. 42 (1985) 185.
[15] P.A. McMurtry, W.H. Jou, J.J. Riley, R.W. Metcalfe, Direct numerical simulations of a reacting mixing layer with chemical heat release, AIAA J. 24 (1986) 962.
[16] W.E. Mell, K.B. McGrattan, H.R. Baum, Numerical simulation of combustion in fire plumes, in: Proceedings of the Twenty-Sixth Symposium (International) on Combustion, The Combustion Institute, 1996, p. 1523.
[17] P. Moin, K. Squires, W. Cabot, S. Lee, A dynamic dubgrid-dcale model for compressible turbulence and scalar transport, Phys. Fluids 3 (1991) 2746.
[18] Y. Morinishi, T.S. Lund, O.V. Vasilyev, P. Moin, Fully conservative higher order finite difference schemes for incompressible flow, J. Comput. Phys. 143 (1998) 90.

[19] C.J. Mueller, J.F. Driscoll, D.L. Reuss, M.C. Drake, M.E. Rosalik, Vorticity generation and attenuation as vortices convect through a premixed flame, Combust. Flame 112 (1998) 342.
[20] H.N. Najm, P.S. Wyckoff, Premixed flame response to unsteady strain rate and curvature, Combust. Flame 110 (1997) 92.
[21] H.N. Najm, P.S. Wyckoff, O.M. Knio, A semi-implicit numerical scheme for reacting flows, i. stiff chemistry, J. Comput. Phys. 143 (1998) 381.
[22] F. Nicoud, Conservative high-order finite-difference schemes for low mach number flows, J. Comput. Phys. 158 (2000) 71.
[23] Ch.D. Pierce, Progress-variable approach for large-eddy simulation of turbulent combustion, Ph.D. thesis, Stanford University, 2001.
[24] T. Poinsot, D. Veynante, Theoretical and Numerical Combustion, Edwards, Philadelphia, 2001.
[25] T. Poinsot, D. Veynante, S. Candel, Quenching processes and premixed turbulent combustion diagram, J. Fluid Mech. 228 (1991) 561.
[26] R.G. Rehm, H.R. Baum, The equations of motion for thermally driven, buoyant flows, J. Res. NBS 3 (1978) 297.
[27] C.M. Rhie, W.L. Chow, A numerical study of the turbulent flow past an airfoil with trailing edge separation, AIAA J. 21 (1983) 1525.
[28] S. Venkateswaran, L. Merkle, Analysis of preconditioning methods for the euler and Navier–Stokes equations, Von Karman Lecture Series, 1999-03, 1999.
[29] W.P. Wang, R.H. Pletcher, On the large-eddy simulation of a turbulent channel flow with significant heat transfer, Phys. Fluids 8 (1996) 3354.